nature
biotechnology

High-throughput measurement of single-cell growth rates using serial microfluidic mass sensor arrays

Nathan Cermak[1,12], Selim Olcum[2,12], Francisco Feijó Delgado[2,3], Steven C Wasserman[3], Kristofor R Payer[4], Mark A Murakami[5], Scott M Knudsen[3], Robert J Kimmerling[3], Mark M Stevens[6], Yuki Kikuchi[4,11], Arzu Sandikci[2], Masaaki Ogawa[7], Vincent Agache[8], François Baléras[8], David M Weinstock[5,9] & Scott R Manalis[1–4,10]

Methods to rapidly assess cell growth would be useful for many applications, including drug susceptibility testing, but current technologies have limited sensitivity or throughput. Here we present an approach to precisely and rapidly measure growth rates of many individual cells simultaneously. We flow cells in suspension through a microfluidic channel with 10–12 resonant mass sensors distributed along its length, weighing each cell repeatedly over the 4–20 min it spends in the channel. Because multiple cells traverse the channel at the same time, we obtain growth rates for >60 cells/h with a resolution of 0.2 pg/h for mammalian cells and 0.02 pg/h for bacteria. We measure the growth of single lymphocytic cells, mouse and human T cells, primary human leukemia cells, yeast, *Escherichia coli* and *Enterococcus faecalis*. Our system reveals subpopulations of cells with divergent growth kinetics and enables assessment of cellular responses to antibiotics and antimicrobial peptides within minutes.

Single cells vary widely in their growth rates, a fundamental phenotype that reflects biochemical and biophysical differences between cells and may govern their relative abundance within a population. From bacteria to unicellular eukaryotes to metazoan cells, even genetically identical cells may grow at different rates owing to a combination of intrinsic molecular noise and various deterministic behavioral programs[1–5]. This variation is not observable via population-based growth assays but has important consequences for human health. For example, cancer cells within an individual may vary drastically in proliferative potential, with subsets capable of continuous cycling and others primarily arrested[6]. Similarly, growth-rate variation in bacterial populations can dictate the efficacy of antibiotic treatments, as slow- or nongrowing cells tend to be more resistant to antibiotics[7–9]. Despite its importance, precise and rapid quantification of single-cell growth rates remains technically challenging. One approach is to measure a cell's outline in a microscopic image and calculate its volume on the basis of assumptions about its three-dimensional shape—e.g., measuring the length of rod-shaped bacteria and assuming the cross-section stays constant[9–12] or measuring yeast cell boundaries and assuming the cell is a prolate ellipsoid[13]. However, it is not clear how often these shape assumptions are violated, and these methods are generally not usable for irregularly shaped cells. Another approach, quantitative phase microscopy, can be used to estimate a cell's dry mass over time[14,15] but, like other available platforms, it cannot perform precise, single-cell growth measurements on a variety of samples with high temporal resolution.

Recently, inertial methods for measuring single-cell growth have been developed on the basis of resonating micromechanical structures[16–18], some of which provide much higher precision than microscopy but are hindered by low throughput. These methods exploit the fact that a micromechanical resonator's natural frequency depends on its mass. Adding cells to a resonator alters the resonator's mass and causes a measurable change in resonant frequency. One such class of resonator mass sensor is the suspended microchannel resonator (SMR), which consists of a sealed microfluidic channel that runs through the interior of a cantilever resonator. The cantilever itself is housed in an on-chip vacuum cavity, reducing damping and improving frequency (and thus mass) resolution[19]. As a cell in suspension flows through the interior of the cantilever, it transiently changes the cantilever's resonant frequency in proportion to the cell's buoyant mass (the mass of the cell minus the mass of the fluid it displaces). In water, a cell's buoyant mass is roughly proportional to (and is typically about one-quarter of) its dry mass[20]. SMRs are very precise, weighing single mammalian cells with a resolution of 0.05 pg (0.1% of a cell's buoyant mass) or better[15–17]. It is possible to measure a cell's growth rate by repeatedly flowing the cell back and forth through the SMR cantilever, but this method is limited to one cell at a time. This limitation in throughput has prevented wider application of SMRs across a range of biological and clinical efforts.

Here we introduce an SMR-based technique that enables high-throughput growth-rate measurement while retaining the precision of the SMR. We use an array of SMRs fluidically connected in series

---

[1]Program in Computational and Systems Biology, Massachusetts Institute of Technology, Cambridge, Massachusetts, USA. [2]Koch Institute for Integrative Cancer Research, Massachusetts Institute of Technology, Cambridge, Massachusetts, USA. [3]Department of Biological Engineering, Massachusetts Institute of Technology, Cambridge, Massachusetts, USA. [4]Microsystems Technology Laboratories, Massachusetts Institute of Technology, Cambridge, Massachusetts, USA. [5]Department of Medical Oncology, Dana-Farber Cancer Institute, Harvard Medical School, Boston, Massachusetts, USA. [6]Department of Biology, Massachusetts Institute of Technology, Cambridge, Massachusetts, USA. [7]Innovative Micro Technology, Goleta, California, USA. [8]CEA-LETI, Minatec Campus, Grenoble, France. [9]Broad Institute, Cambridge, Massachusetts, USA. [10]Department of Mechanical Engineering, Massachusetts Institute of Technology, Cambridge, Massachusetts, USA. [11]Present address: Hitachi High-Technologies Corporation, Ibaraki-ken, Japan. [12]These authors contributed equally to this work. Correspondence should be addressed to S.R.M. (srm@mit.edu).

and separated by 'delay' channels (**Fig. 1a,b**). These delay channels give the cell time to grow as it flows between cantilevers. After a cell exits a cantilever, other cells are free to enter it and be weighed. As a result, we are not limited to flowing only one cell through the array at a time but can have many cells flowing in a queue. This enables high-throughput precision growth measurements across a wide array of suspended cell types. Here we demonstrate a proof-of-concept serial SMR array and show that it can measure lymphoid cell lines, primary mouse T cells, primary human lymphocytes and acute myeloid leukemia cells, *Saccharomyces cerevisiae*, *E. coli* and *E. faecalis*. We demonstrate previously unrecognized variability in growth kinetics and perform ultra-rapid assessment of susceptibility to antibiotics and antimicrobial peptides.

RESULTS
Device design
Before designing the serial SMR arrays, we first considered how the number of buoyant mass measurements (k), measurement resolution (σ_{mass}) and the time between measurements (Δt) affect the resolution of the mass accumulation rate. We derived a simple relationship for the standard error (resolution) of the mass accumulation rate in terms of these three quantities:

$$\sigma_{mass\,accumulation\,rate} \approx \frac{\sigma_{mass}\sqrt{12}}{k^{1.5}\Delta t} \qquad (1)$$

(see **Supplementary Note 1** for derivation).

For serial SMR arrays, Δt can be controlled by adjusting the flow rate. Therefore, apart from guiding our designs, equation (1) also illustrates that we can easily tune the device's behavior to trade throughput for resolution by changing the flow rate; i.e., faster flow yields higher throughput but poorer resolution, and vice versa for slower flow (**Supplementary Note 1**).

In this work, we designed and validated two serial SMR arrays with different channel dimensions—one for larger cells (mammalian cells and yeast, $15 \times 20\ \mu m$ in cross-section) and one for bacteria ($3 \times 5\ \mu m$). Despite the differences in scale, the operation and design concepts for these devices are essentially identical.

For studying mammalian and yeast cells, which often accumulate mass at rates of 1–10 pg/h (ref. 16), we sought a mass accumulation rate resolution of <1 pg/h. Using the expected mass noise (σ_{mass} ~0.05 pg for similar single-SMR devices), we designed a device consisting of 12 SMRs fluidically connected in series by delay channels ~50 mm long (**Fig. 1b**). At typical SMR flow rates, Δt would be about 1.5 min, and the expected mass accumulation rate resolution would thus be 0.17 pg/h, resulting in a relative precision of 1–10%. We designed our small-channel devices similarly, but with 10 cantilevers and with the expectation of operating at faster flow rates (Δt ~30 s between SMRs).

To obtain the best possible mass resolution (σ_{mass}), we excited cantilevers in the second bending mode (**Fig. 1c**) so that the measured mass would not depend on the cell's flow path[21], thus avoiding a fundamental source of error for SMRs operated in the first mode. However, because the second mode is at a higher frequency, and the tip follows an arc with a shorter radius than in the first mode, cells often became trapped at the cantilever tip owing to centrifugal force[22,23]. This problem was exacerbated at the low flow rates (and therefore reduced drag forces) necessary for sufficient delay time between cantilevers. To overcome the trapping problem, we shortened the interior channel to extend only as far as the vibration node, where the centrifugal force is minimal (**Fig. 1c**).
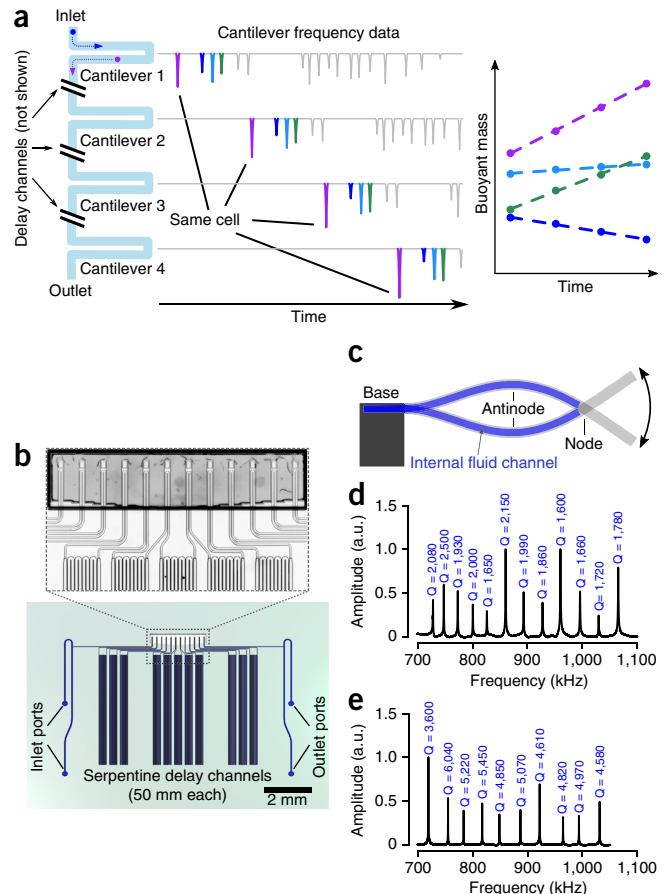
Figure 1 Design and implementation of the serial SMR array. (**a**) Simulated data showing frequency peaks originating from single cells flowing through a series of SMRs (cantilever mass sensors) separated by delay channels. Cells grow as they traverse the array. After frequency peaks originating from the same cell are grouped, that cell's mass accumulation rate can be obtained by regressing its buoyant mass versus time. Because many cells can traverse the array simultaneously, this device can achieve much higher throughput than a single SMR device. (**b**) Rendering of a large-channel serial SMR array device showing delay channels and the cantilevers (magnified in inset micrograph). (**c**) Side-view illustration of an SMR vibrating in the second bending mode. To prevent cells from getting trapped at the end of the cantilever by large centrifugal forces, the internal microfluidic channel (blue) extends only to the node of the second eigenmode. (**d**) Transfer function amplitude measured a large-channel serial SMR array, demonstrating frequency spacing of approximately 30 kHz and typical quality factors of 1,500–2,500. (**e**) Transfer function for a small-channel serial SMR array. a.u., arbitrary units.

So that each cantilever could be operated individually without coupling or interacting with other cantilevers, we used frequency-division multiplexing. We designed each cantilever with a unique resonant frequency roughly 30 kHz apart from that of its neighbors (**Fig. 1d,e**), which we controlled by varying cantilever lengths from 380 to 470 μm (large-channel devices) or from 180 to 215 μm (small-channel devices). This frequency spacing is conservative, as we estimate on the basis of Carson's rule[24] that the spacing could be reduced to less than 1 kHz in future devices, enabling operation of hundreds of cantilevers simultaneously within the frequency band used here (700–1,100 kHz).

Device operation and data analysis
To simultaneously measure the resonant frequency of all k cantilevers in the array, we first needed to measure the superposition of all the

cantilever deflection signals. We employed two approaches: (i) an optical lever setup, in which all cantilevers are simultaneously illuminated and a single photodetector measures the superposition of their deflection signals (**Supplementary Fig. 1**), or (ii) using devices with piezoresistors doped into the base of each cantilever[22,25], which are wired in parallel and their combined resistance measured via a Wheatstone bridge–based amplifier. The resulting deflection signal, which consists of the sum of k signals from the cantilever array, goes to an array of k phase-locked loops (PLLs) where each PLL locks to the unique resonant frequency of a single cantilever. Therefore there is a one-to-one pairing between cantilevers and PLLs. Each PLL determines its assigned cantilever's resonant frequency, by demodulating its deflection signal[26], then generates a sinusoidal drive signal at that frequency. The drive signals from each PLL are summed and used to drive a single piezoceramic actuator positioned directly underneath the chip, completing the feedback loop (**Supplementary Fig. 1**). Each PLL is configured such that it will track its cantilever's resonant frequency with a bandwidth of 50 or 100 Hz (Online Methods and **Supplementary Fig. 2**).

After acquiring the frequency signals for each cantilever, we convert them to mass units via each cantilever's sensitivity (Hz/pg), which must be known precisely. Although cantilever mass sensitivity should theoretically scale with the resonant frequency f to the power of 3/2 ($f^{3/2}$) (**Supplementary Note 2**), we found that the actual sensitivities occasionally deviated from the expected values and in some cases changed by up to 5% between days (**Supplementary Fig. 3**). To account for this, we measured the cantilever sensitivities during each experiment by spiking in inert monodisperse polystyrene–particle size standards into all samples. Because the particles are highly uniform (~1% coefficient of variation in diameter), we can easily distinguish them even when they are of similar size to the cells of interest.

The final step in extracting individual cell mass accumulation rates is to identify the frequency peaks in each cantilever that originate from the same cell. This is easily accomplished if the cells stay in the same order as they flow through the array. In practice, however, cells occasionally change order, divide or drop out of the queue (by adhering to a channel wall or getting physically stuck in the channel) and may re-enter the queue at a later time. To match frequency peaks to the cells that generated them, we use a probabilistic model based on our assumptions about the expected time for a cell to traverse a delay channel and about the fastest rates at which cells can change mass. We assume that mass accumulation rates are nearly constant on the timescale of our measurements, which constitute a small fraction of a cell cycle[16,17] (**Supplementary Note 3** and **Supplementary Fig. 4**). We then apply the Hungarian algorithm[27] to find a maximally likely way of matching all the cell events observed in cantilever 2 with the cells that have been observed in cantilever 1, followed by matching the cells observed in cantilever 3 with the cells observed in cantilevers 1 and 2, and so on. At concentrations used here, the matching is robust (better than 99% for simulated data; **Supplementary Fig. 5**), and can be manually verified for accuracy. At higher cell concentrations, the risk of incorrect matching increases, but outliers of interest can still be manually verified.

Device characterization

As these devices represent the first chips implementing SMR arrays, we asked whether operating 10–12 cantilevers simultaneously would decrease the performance of each cantilever. We measured the frequency noise for 12 large-channel cantilevers operating simultaneously using an optical-lever-based measurement system and observed minimal frequency noise (in terms of Allan deviations[28]) of 20–30 parts per billion at averaging times of 200–500 ms (**Supplementary Fig. 6**). Slightly lower Allan deviations were observed for small-channel devices (**Supplementary Fig. 6**), with optimal noise at shorter averaging times (30–100 ms). In both cases, these noise magnitudes are comparable to that routinely achieved with single-cantilever devices but have the potential to be further reduced—by an order of magnitude or more—before reaching thermomechanical limits (**Supplementary Fig. 6**).

To assess how well the devices could resolve a cell's mass accumulation rate, we first analyzed mixtures of polystyrene particles spanning 4–12 µm in diameter for large-channel devices and 1.0–2.5 µm
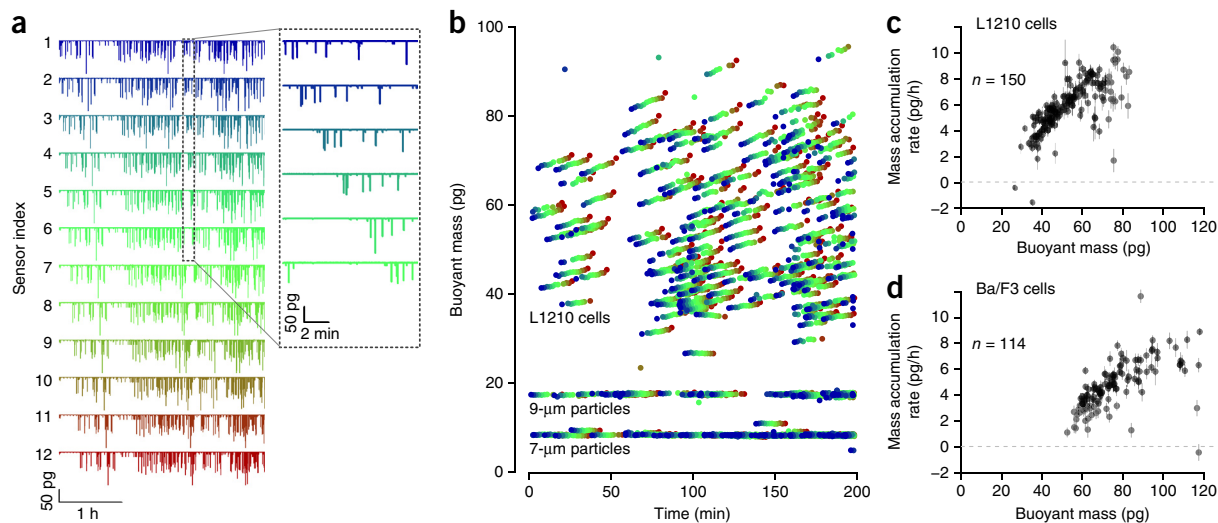
Figure 2 Measuring the growth of lymphoid cell lines. (**a**) Data from 12 cantilevers demonstrating continuous operation over roughly 3 h with L1210 cells at a flow rate of roughly 2 min between each cantilever (inset). (**b**) Buoyant mass data for L1210 cells extracted from frequency shifts of cantilevers; each color corresponds to a single cantilever, color-coded as in **a**. 7-µm particles were added as calibration; 9-µm particles were added as negative control (both are inert polystyrene particles). (**c**) Buoyant mass versus mass accumulation rate for L1210 cells in **b**, extracted via an automated peak-matching algorithm (**Supplementary Note 3**). Error bars indicate standard errors of the slope estimated directly from the fit. (**d**) Buoyant mass versus mass accumulation rate for Ba/F3 cells, showing a profile similar to that of L1210 cells but at larger cell sizes.
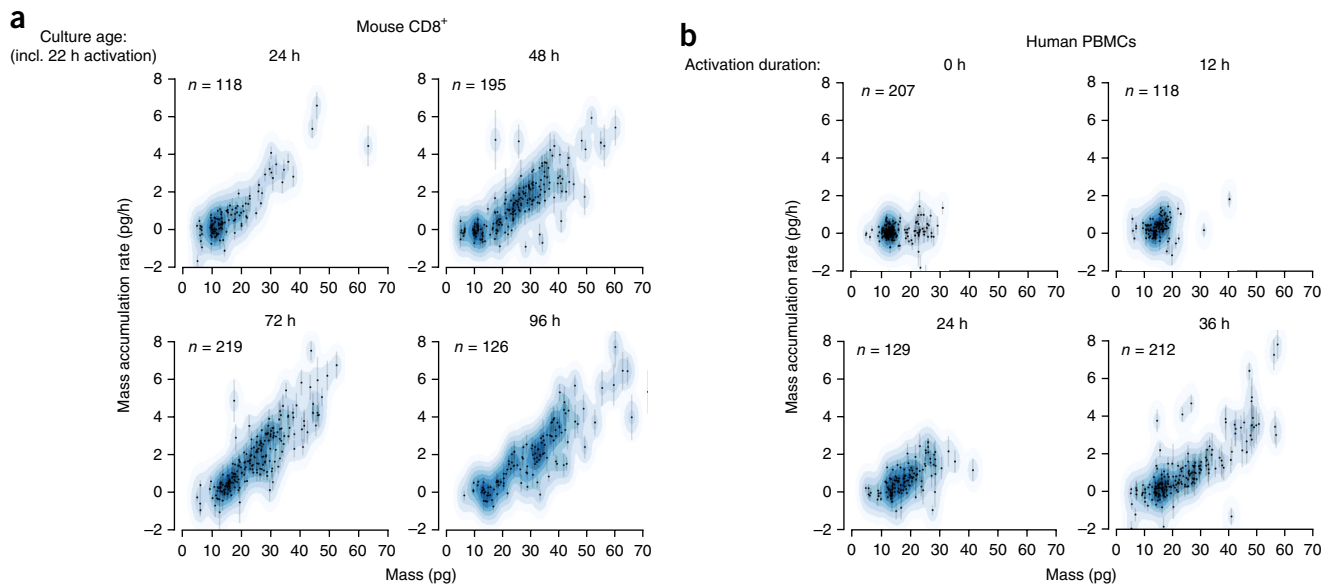
Figure 3 Measuring single immune-cell growth patterns and activation dynamics. (**a**) Mass accumulation rate over time in mouse CD8+ T cells activated with anti-CD3 and anti-CD28. Error bars indicate standard error of the slope, estimated directly from the regression fit. Points are overlaid on corresponding kernel density estimates (blue). (**b**) Lymphocyte activation, measured by quantifying mass and growth of single human PBMCs.

for small-channel devices. Our measurements clearly showed that these particles' masses were not changing, and the s.d. of the observed rates (an estimate for mass accumulation rate resolution) were 0.32 pg/h for the large-channel device (**Supplementary Fig. 7**) and 0.022 pg/h for the small-channel device (**Supplementary Fig. 8**). We also tested the large-channel device with fixed cells, which did not change in mass and showed a similarly low mass accumulation rate s.d. of 0.18 pg/h (**Supplementary Fig. 9**). These results are in agreement with what we would predict from equation (1) on the basis of the experimental flow rates and measured buoyant mass resolution.

Measuring growth rates of living cells

We used the large-channel serial SMR array to monitor the growth of steady-state L1210 cells (**Fig. 2**), a mouse lymphoblast cell line previously studied with SMRs[16,17]. In a 200-min experiment, we measured the size and mass accumulation rate of 150 cells. In the same time frame, a single SMR measuring each cell for 20 min could measure fewer than 10 cells, as it takes some time to switch between cells. As seen previously, these cells' mass accumulation rates were size-dependent and were higher for larger cells (**Fig. 2c**). We also measured Ba/F3 pro-B cells expressing the BCR–ABL oncoprotein. Under the same conditions as for the L1210 cells, we found a similar correlation
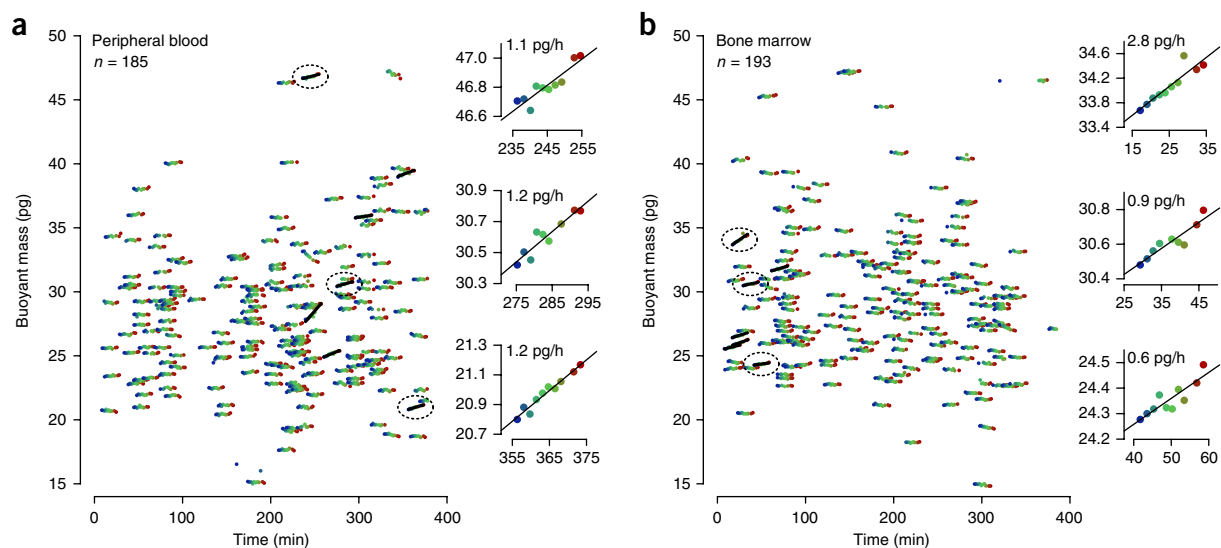
Figure 4 Measuring growth dynamics of single hCD15+hCD33+ AML cells from two patients. (**a**) Mass over time plotted for cells from a peripheral blood draw (**a**) or bone marrow (**b**). Cells with statistically significant growth (*P* < 0.001, one-sided *t*-test for slope > 0) are marked with black lines; insets show data for three growing cells. Not shown are 7-μm (~8.5 pg) particles included in these samples for calibration. Data from the first cantilever were not used in this analysis owing to abnormally high noise; **a** and **b** each reflect data from one (distinct) patient.

between mass and mass accumulation rate (**Fig. 2d**). As previously shown for L1210 cells[17] but not Ba/F3 cells, the mass accumulation rate per unit cell mass is lower for smaller cells compared to larger cells, suggesting that Ba/F3 cells also deviate from purely exponential growth in a manner similar to L1210s.

We next investigated whether we could measure primary cells, beginning with mouse CD8^{+} T cells. CD8^{+} T cells are known to drastically alter their metabolic activity and begin to grow in response to stimulation[29]. However, current methods for studying this transition often rely on bulk or single-time-point measurements, which makes it difficult to characterize heterogeneity in this phenotypic response over time. To this end, we activated mouse CD8^{+} T cells *in vitro* and assayed their single-cell growth behavior daily for 4 d. Although the cumulative cell population grew robustly between daily measurements, the serial SMR consistently revealed a sizable nongrowing subpopulation (**Fig. 3a**) composed of the lowest-weight fractions (5–15 pg buoyant mass). Between 24 and 48 h, the growing subpopulation increased relative to the nongrowers and stayed roughly constant in size after 48 h. As with L1210 and Ba/F3 cells, although the mass accumulation rate covaried with size in all cases, it was not directly proportional to mass but was instead proportional to mass minus an offset. This departure from exponential growth is similar to that seen for the L1210 and Ba/F3 cells.

Our measurements of mouse CD8^{+} T cells suggested we could rapidly assess human lymphocyte activation as an alternative to clinical techniques such as the lymphocyte transformation test[30,31]. This assay measures proliferation via DNA synthesis—typically via incorporation of tritiated thymidine—and requires several days to quantify bulk proliferation in response to activation. In contrast, we could directly observe activated lymphocytes within a population of unlabeled peripheral blood mononuclear cells (PBMCs) within 24–36 h after stimulation. We obtained PBMCs from whole blood, activated them for varying durations and then immediately measured their growth (**Fig. 3b**). Naive (*t* = 0 h) PBMCs show a clear subpopulation of cells between 20 and 30 pg, but this subpopulation was not detectable after 12 h of activation, consistent with monocyte adherence to the culture dish[32]. By 24 h, larger growing cells (putative activated T cells) were present, and by 36 h this population had expanded to even larger sizes and faster mass accumulation rates. The ability to assess growth within 36 h by mass accumulation of individual cells suggests the serial SMR array could provide a substantially faster method for assessing lymphocyte transformation than existing approaches that measure proliferation. Furthermore, quantitatively assessing single-cell growth within highly heterogeneous populations could help to identify responsive clones in a population of generally unresponsive cells. This functionality is particularly promising for fields such as cancer immunotherapy, where the characterization of rare, responsive lymphocytes may offer crucial insight for the identification of tumor neoantigens.

To further explore the capabilities of the system for studying primary cell growth kinetics, we asked whether we could detect growth in single putative cancer cells from patients. We enriched acute myeloid leukemia cells from the peripheral blood or bone marrow of two patients by flow sorting cells expressing human CD15 and CD33 (hCD15^{+}hCD33^{+}) (**Supplementary Fig. 10** and **Supplementary Table 1**), which were then maintained in serum-supplemented medium. In neither case was the tumor immunophenotype known in advance, so the collected cell populations were heterogeneous owing to the conservative sorting strategy. Although no growth was visible at the population level over the first 48 h (**Supplementary Fig. 11**), we detected a rare subpopulation of cells (~4% of each sample)
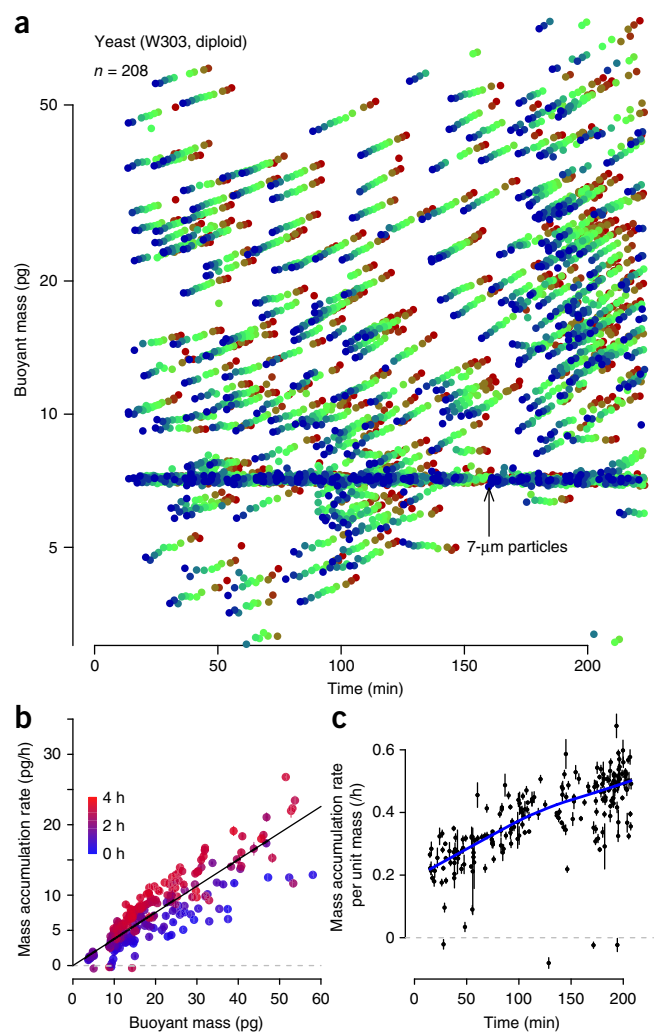
Figure 5 Measuring lag-phase yeast culture time-resolved growth dynamics at single-cell resolution. (**a**) Semilog plot of buoyant mass trajectories of yeast cells in rich medium. Data from SMR 9 were not used owing to very high noise. Particles between 5 and 20 pg are probably mostly single cells; particles with mass >20 pg are mostly clumps of cells. (**b**) Buoyant mass versus mass accumulation rate. Error bars indicate standard error of the slope estimated from each regression of buoyant mass versus time. (**c**) Mass accumulation rate per unit mass (interpretable as exponential growth rate) versus time. Error bars indicate standard error of the slope divided by the cell's buoyant mass. Blue line shows locally weighted scatterplot smoothing (LOWESS) curve.

that were accumulating mass when we analyzed these samples on the serial SMR array 3–9 h after sample acquisition (**Fig. 4**). These cells typically grew between 0.2 and 1 pg over the 20-min measurement, which would correspond to a <1% change in diameter. We also noted another rare subpopulation of cells losing mass, which may be in the process of dying. These data—though exploratory—show that the serial SMR can resolve heterogeneous growth patterns in primary patient samples.

We next investigated whether the large-channel serial SMR array could be used to study *S. cerevisiae,* a model organism of interest in studies of growth-rate control and size homeostasis[3,13]. We measured the growth of single yeast cells in lag phase—a brief period of slow or no growth after transfer from spent medium to fresh medium. In a 3.5-h experiment, we measured the mass accumulation rates of
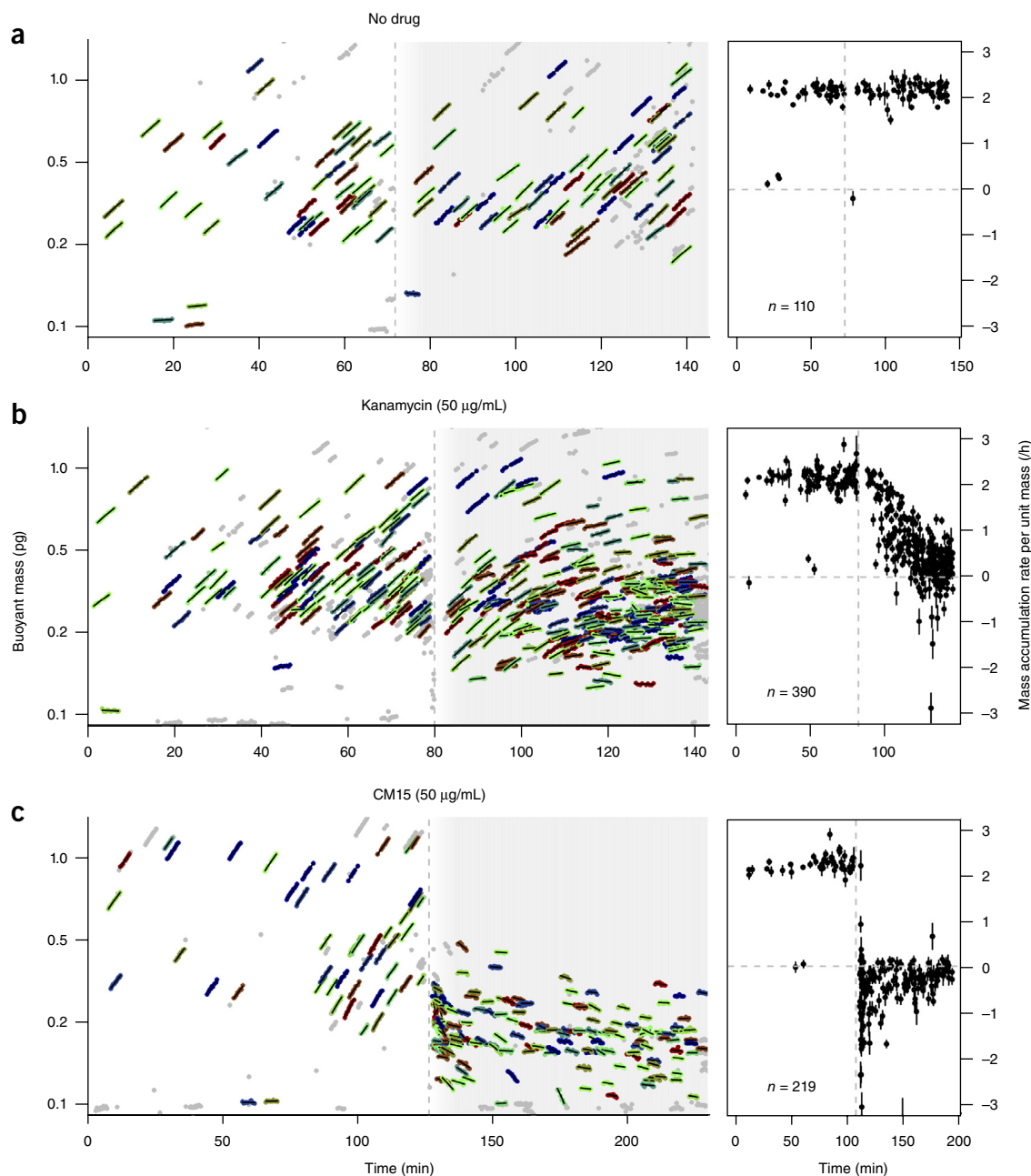
Figure 6 Measuring bacterial growth and drug response on a small-channel serial SMR array. (**a–c**) Serial SMR array buoyant mass measurements (left) and plots of mass accumulation rate per unit mass versus time (right) for *E. coli* cultures without drug (**a**) or in the presence of kanamycin (**b**) or CM15 (**c**). Colored dots with overlaid lines (left) indicate cells included in the analysis at right; gray dots indicate data for which <6 mass measurements could be linked together or the automated matching was uncertain. Data from polystyrene particles used for calibration were omitted for clarity. Error bars indicate standard errors of regression parameter for normalized growth rate. Vertical dashed lines indicate the time at which a drug was added (**b,c**).

208 cells (or cell clumps, as daughter cells often remain adhered to mother cells after division) (**Fig. 5**). We plotted these cells' masses on a logarithmic scale because single yeast cells grow exponentially[3,16]. On a semilog plot the slope of a cell's mass trajectory may be interpreted as an exponential growth rate, which is equivalent to its mass accumulation rate per unit mass. Below we refer to this as the cell's growth rate. Throughout the first several hours following inoculation into fresh medium, the cell growth rates increased toward their maximal rate of approximately 0.5 per hour (**Fig. 5b,c**). Notably, the initial growth rate (i.e., immediately after inoculation into fresh medium)

was not 0 but rather around 0.2/h, showing that yeast in stationary phase remain primed to begin growing immediately, albeit at a submaximal rate, should conditions become favorable.

We next asked whether serial SMR arrays designed for bacteria could provide rapid and precise measurements of bacterial growth. We first investigated the growth of single log-phase *E. coli* cells (**Fig. 6a**). In rich medium (LB) at 37 °C, the average growth rate of individual bacteria was 2.14 ± 0.02/h (mean ± s.e.m., 19.4 min doubling time) with a coefficient of variation of 7.4% excluding four outlying small cells (**Fig. 6a**), in good agreement with other recent measurements[12].

However, it is notable that we were measuring growth on a much shorter timescale (4 min instead of a full 20-min cell cycle) and that the biological variation on this timescale was no larger than at longer timescales. We were also able to measure growth of the Gram-positive coccus *E. faecalis* (**Supplementary Fig. 12**). This strain behaved similarly to the Gram-negative rod *E. coli* in the serial SMR array, growing at easily detectable rates with a mean of 1.86 ± 0.02/h. The serial SMR array can thus provide high-resolution and rapid growth measurements of single Gram-positive and Gram-negative bacteria of varying morphologies, including clinically relevant species.

We next asked whether we could observe the effects of antibiotics on bacterial growth. We added kanamycin to an *E. coli* culture midway through the experiment (**Fig. 6b**), after which the growth rate dropped rapidly, reaching almost 0 in less than 0.5 h. This result demonstrates the potential for assessment of antibiotic susceptibility and quantification of killing kinetics on an unprecedented timescale. Furthermore, we noted variation in the timescale of growth arrest: after 20 min of exposure to kanamycin, some cells had nearly stopped growing while others continued growing near their maximal rate.

Finally, we asked whether we could observe the growth-arresting effects of the antimicrobial peptide CM15 (ref. 33), which is known to permeabilize cells on short timescales but does not change the overall cell size as measured by microscopy[34]. When we added CM15 to the *E. coli* culture, we observed an immediate decrease in mean cell mass and an immediate cessation of mass accumulation (**Fig. 6c**). Although most cells appeared to be neither growing nor decreasing in mass, we observed rapid loss of mass in several cells immediately after peptide addition and up to nearly 1 h later.

DISCUSSION

We have shown that the serial SMR array can precisely measure single-cell mass accumulation rates for up to 60 mammalian or 150 bacterial cells per hour. This enables observation of the full distribution of growth behaviors—including rare cells behaving very differently from the average cell—on short timescales. This method is compatible with a variety of cell types, including cell lines, primary blood cells, yeast and bacteria, and can be used to profile the response of cells in culture to perturbations, including small-molecule therapeutics and peptides. We envision that this device will be applicable in many areas of research and potentially in a clinical setting. The ability to detect rare growing cells in complex mixtures from patients suggests the possibility of correlating these types of measurements to disease states and assessing drug susceptibility in these rare cells. Outside of medical applications, the serial SMR system could be used to quantify cellular heterogeneity to determine how cell growth is intrinsically tied to a broad array of molecular-scale phenomena.

Our system has both benefits and drawbacks compared to microscopy, which has long been a mainstay for studying cell growth. Small-channel serial SMR arrays provide at least tenfold higher precision than that reported in a recent quantitative phase microscopy study[35] (**Supplementary Note 4** and **Supplementary Fig. 13**). Furthermore, at slower flow rates, the precision increases by another two- to three-fold, to a level achievable with dynamic trapping measurements performed on a single SMR (**Supplementary Fig. 13**). This higher resolution is probably the reason we observed substantially less cell-to-cell variability (**Supplementary Fig. 13b,d**). The high precision applies to cells in flow, including motile cells, which is advantageous for automated clinical assays such as antibiotic-susceptibility testing; however, there are drawbacks to our method. The serial SMR array is currently not suitable for measuring growth of cells that are attached to a surface. Furthermore, unlike microscopy, this method can capture only short 'snapshots' of single-cell growth, though the length of the snapshot may increase in the future with increasing SMR parallelization. Finally, microscopes are more widely available and easier to operate than the current version of our serial SMR system.

In future work, the serial SMR approach described here could be optimized further. Improving the actuation and detection schemes might reasonably enable an order-of-magnitude improvement in mass accumulation rate precision (**Supplementary Fig. 6**), and this extra precision could be exchanged directly for higher throughput by increasing the flow rates of cells transiting the array (**Supplementary Note 1** and **Supplementary Fig. 14**). Another possibility is to further parallelize the system by implementing many serial SMR arrays on a single chip, enabling measurement of cells under many conditions simultaneously—for example, bacteria in several different concentrations of antibiotic. Other future advancements could include integration with fluorescence microscopy and methods to sort cells on the basis of growth rate, both of which would greatly expand the potential for correlative assays that link growth kinetics with underlying biology.

METHODS

Methods and any associated references are available in the online version of the paper.

Note: Any Supplementary Information and Source Data files are available in the online version of the paper.

AUTHOR CONTRIBUTIONS
N.C., S.O. and F.F.D. designed devices; N.C., S.O. and S.C.W. designed and constructed the experimental setup; K.R.P., M.O., V.A. and F.B. fabricated the devices; N.C., S.O., M.M.S., R.J.K., S.M.K., A.S., Y.K., D.M.W. and S.R.M. designed the experiments, N.C., S.O., S.M.K., R.J.K., M.A.M. and M.M.S. performed the experiments; N.C. analyzed the data; N.C., S.O. and S.R.M. wrote the paper with input from all authors.

COMPETING FINANCIAL INTERESTS
The authors declare competing financial interests: details are available in the online version of the paper.

Reprints and permissions information is available online at http://www.nature.com/reprints/index.html.

1. Labhsetwar, P., Cole, J.A., Roberts, E., Price, N.D. & Luthey-Schulten, Z.A. Heterogeneity in protein expression induces metabolic variability in a modeled *Escherichia coli* population. *Proc. Natl. Acad. Sci. USA* **110**, 14006–14011 (2013).
2. Balaban, N.Q., Merrin, J., Chait, R., Kowalik, L. & Leibler, S. Bacterial persistence as a phenotypic switch. *Science* **305**, 1622–1625 (2004).
3. Di Talia, S., Skotheim, J.M., Bean, J.M., Siggia, E.D. & Cross, F.R. The effects of molecular noise and size control on variability in the budding yeast cell cycle. *Nature* **448**, 947–951 (2007).
4. van Heerden, J.H. *et al.* Lost in transition: start-up of glycolysis yields subpopulations of nongrowing cells. *Science* **343**, 1245114 (2014).

5. Sandler, O. *et al.* Lineage correlations of single cell division time as a probe of cell-cycle dynamics. *Nature* **519**, 468–471 (2015).
6. Reya, T., Morrison, S.J., Clarke, M.F. & Weissman, I.L. Stem cells, cancer, and cancer stem cells. *Nature* **414**, 105–111 (2001).
7. Keren, I., Kaldalu, N., Spoering, A., Wang, Y. & Lewis, K. Persister cells and tolerance to antimicrobials. *FEMS Microbiol. Lett.* **230**, 13–18 (2004).
8. Fridman, O., Goldberg, A., Ronin, I., Shoresh, N. & Balaban, N.Q. Optimization of lag time underlies antibiotic tolerance in evolved bacterial populations. *Nature* **513**, 418–421 (2014).
9. Aldridge, B.B. *et al.* Asymmetry and aging of mycobacterial cells lead to variable growth and antibiotic susceptibility. *Science* **335**, 100–104 (2012).
10. Wang, P. *et al.* Robust growth of *Escherichia coli*. *Curr. Biol.* **20**, 1099–1103 (2010).
11. Moffitt, J.R., Lee, J.B. & Cluzel, P. The single-cell chemostat: an agarose-based, microfluidic device for high-throughput, single-cell studies of bacteria and bacterial communities. *Lab Chip* **12**, 1487–1494 (2012).
12. Taheri-Araghi, S. *et al.* Cell-size control and homeostasis in bacteria. *Curr. Biol.* **25**, 385–391 (2015).
13. Ferrezuelo, F. *et al.* The critical size is set at a single-cell level by growth rate to attain homeostasis and adaptation. *Nat. Commun.* **3**, 1012 (2012).
14. Barer, R. Interference microscopy and mass determination. *Nature* **169**, 366–367 (1952).
15. Zangle, T.A. & Teitell, M.A. Live-cell mass profiling: an emerging approach in quantitative biophysics. *Nat. Methods* **11**, 1221–1228 (2014).
16. Godin, M. *et al.* Using buoyant mass to measure the growth of single cells. *Nat. Methods* **7**, 387–390 (2010).
17. Son, S. *et al.* Direct observation of mammalian cell growth and size regulation. *Nat. Methods* **9**, 910–912 (2012).
18. Park, K. *et al.* Measurement of adherent cell mass and growth. *Proc. Natl. Acad. Sci. USA* **107**, 20691–20696 (2010).
19. Burg, T.P. *et al.* Vacuum-packaged suspended microchannel resonant mass sensor for biomolecular detection. *J. Microelectromech. Syst.* **15**, 1466–1476 (2006).
20. Feijó Delgado, F. *et al.* Intracellular water exchange for measuring the dry mass, water mass and changes in chemical composition of living cells. *PLoS One* **8**, e67590 (2013).
21. Lee, J., Bryan, A.K. & Manalis, S.R. High precision particle mass sensing using microchannel resonators in the second vibration mode. *Rev. Sci. Instrum.* **82**, 023704 (2011).
22. Lee, J. *et al.* Suspended microchannel resonators with piezoresistive sensors. *Lab Chip* **11**, 645–651 (2011).
23. Lee, J., Shen, W., Payer, K., Burg, T.P. & Manalis, S.R. Toward attogram mass measurements in solution with suspended nanochannel resonators. *Nano Lett.* **10**, 2537–2542 (2010).
24. Carson, J.R. Notes on the theory of modulation. *Proc. Inst. Radio Eng.* **10**, 57–64 (1922).
25. Tortonese, M., Yamada, H., Barrett, R.C. & Quate, C.F. Atomic force microscopy using a piezoresistive cantilever. *Transducers* **1991**, 448–451 (1991).
26. Olcum, S., Cermak, N., Wasserman, S.C. & Manalis, S.R. High-speed multiple-mode mass-sensing resolves dynamic nanoscale mass distributions. *Nat. Commun.* **6**, 7070 (2015).
27. Kuhn, H.W. The Hungarian method for the assignment problem. *Nav. Res. Logist. Q.* **2**, 83–97 (1955).
28. Allan, D.W. Statistics of atomic frequency standards. *Proc. IEEE* **54**, 221–230 (1966).
29. Fox, C.J., Hammerman, P.S. & Thompson, C.B. Fuel feeds function: 934energy metabolism and the T-cell response. *Nat. Rev. Immunol.* **5**, 844–852 (2005).
30. Halpern, B. & Amache, N. Diagnosis of drug allergy in vitro with the lymphocyte transformation test. *J. Allergy* **40**, 168–181 (1967).
31. Poujol, F. *et al.* Flow cytometric evaluation of lymphocyte transformation test based on 5-ethynyl-2'deoxyuridine incorporation as a clinical alternative to tritiated thymidine uptake measurement. *J. Immunol. Methods* **415**, 71–79 (2014).
32. Elkord, E., Williams, P.E., Kynaston, H. & Rowbottom, A.W. Human monocyte isolation methods influence cytokine production from *in vitro*–generated dendritic cells. *Immunology* **114**, 204–212 (2005).
33. Andreu, D. *et al.* Shortened cecropin A-melittin hybrids. Significant size reduction retains potent antibiotic activity. *FEBS Lett.* **296**, 190–194 (1992).
34. Fantner, G.E., Barbero, R.J., Gray, D.S. & Belcher, A.M. Kinetics of antimicrobial peptide activity measured on individual bacterial cells using high-speed atomic force microscopy. *Nat. Nanotechnol.* **5**, 280–285 (2010).
35. Mir, M. *et al.* Optical measurement of cycle-dependent cell growth. *Proc. Natl. Acad. Sci. USA* **108**, 13124–13129 (2011).

ONLINE METHODS

Device design and fabrication. Devices were fabricated using previously described methods[22,36]. Large-channel devices used with optical-lever readout were fabricated at MIT's Microsystems Technology Laboratories and Innovative Micro Technology (IMT), and large-channel devices with embedded piezoresistors for readout were fabricated at CEA–LETI. Notably, the large devices designed for optical-lever readout did not include a getter layer, but the cavity surrounding the cantilevers remained in vacuum. Large-channel devices had cantilever interior channels of $15 \times 20\ \mu m$ in cross-section, and delay channels $20 \times 30\ \mu m$ in cross-section. Only human PBMC measurements were carried out on large-channel devices fabricated at CEA–LETI; all other mammalian cell and yeast experiments were on devices fabricated at IMT without piezoresistors. Small-channel devices were fabricated at IMT and had cantilever channels $3 \times 5\ \mu m$ in cross-section, and delay channels $4 \times 15\ \mu m$ in cross-section. The tips of the cantilevers in the array are aligned (**Fig. 1**) so that a single line-shaped laser beam can be used for optical-lever readout (**Supplementary Fig. 1**). The cantilevers were arrayed such that the shortest (and therefore most sensitive) cantilevers were at the ends of the array. Before use, the device was first cleaned with piranha (3:1 sulfuric acid to 50% hydrogen peroxide) and the channel walls were passivated with polyethylene glycol (PEG) grafted onto poly-L-lysine (SuSoS).

System setup. A full schematic and picture for the device setup using optical-lever based detection is shown in **Supplementary Figure 1**. A piezoceramic actuator seated underneath the device is used for actuation. The custom-made low-noise photodetector, Wheatstone bridge–based amplifier (for piezoresistor readout) and high-current piezoceramic driver have been described elsewhere[37]. It is worth noting that in previous readout systems designed for a single cantilever, signal distortion (via electronic saturation or optical interference patterns) did not typically contribute to system noise, as the distortion generates spectral components at integer multiples of the carrier frequency that are easily filtered out. However, in a channel carrying many signals, nonlinear distortion (especially saturation) will generate noise near the carrier signals (**Supplementary Fig. 15**). Therefore, care must be taken to ensure that no signals become saturated. To avoid the effects of optical interference between signals from different cantilevers (producing harmonics at the difference frequency), we used a low-coherence-length light source (675 nm superluminescent diode, 7 nm full-width half-maximum spectral width, Superlum) for our optical lever. After the custom photodetector converts the optical signal to a voltage signal, the voltage signal is fed into a field-programmable gate array (FPGA) board, for which implementation details were published previously[26]. Briefly, the FPGA implements 12 parallel second-order phase-locked loops that both demodulate and drive a single cantilever. The FPGA is a Cyclone IV FPGA (Altera) on a DE2-115 development board (Terasic Inc.) operating on a 100 MHz clock (AOCJY2 oven-controlled crystal oscillator, Abracon). Analog input and output were via a high-speed analog-to-digital/digital-to-analog (AD/DA) card (DCC HSMC card, Terasic Inc.) operating 14-bit AD and DA converters at 100 MHz.

System operation. To operate all cantilevers in the array, we first measure the resonator array transfer function by sweeping the driving frequency and recording the amplitude and phase of the array response. We next calculate parameters for each PLL such that each cantilever-PLL feedback loop has a 50- or 100-Hz FM-signal bandwidth. We then adjust the phase-delay for each PLL to maximize the cantilever vibration amplitude. Finally, we measure the FM-signal transfer function for each cantilever–PLL feedback loop to confirm sufficient measurement bandwidth (in case of errors in setting the parameters). This transfer function relates the measured cantilever–PLL oscillation frequency to a cantilever's time-dependent intrinsic resonant frequency. Frequency data for each cantilever are collected at 500 Hz, and are transmitted from the FPGA via Ethernet to a personal computer where they are saved via custom LabView software (National Instruments).

As in previous SMR systems, the device is placed on a copper heat sink/source connected to a heated water bath maintained at 30 °C (yeast) or 37 °C (mammalian cells and *E. coli*) for the duration of the experiment. The sample is loaded into the device from vials pressurized under air (yeast and *E. coli*) or air with 5% CO_2 (mammalian cells) (**Supplementary Fig. 1**), through 0.009-inch

inner-diameter fluorinated ethylene propylene (FEP) tubing. The pressurized vials are seated in a temperature-controlled sample holder throughout the measurement. FEP tubing allows us to flush the device with piranha solution for cleaning, as piranha will damage most nonfluorinated plastics. To measure a sample of cells, we first flush the device with filtered medium and then flush the sample into one bypass channel. NIST-traceable polystyrene beads are added to the sample as an internal calibration standard. For experiments on large-channel devices, we typically apply between 1 and 2 p.s.i. across the entire array, yielding flow rates on the order of 0.5 nL/s (the array's calculated fluidic resistance is approximately 3×10^{16} Pa/(m³/s), calculated as described[38]). For small-channel devices, we apply 4–5 p.s.i. across the array, yielding flow rates of ~0.1 nL/s. Additionally, every several minutes we flush new sample into the input bypass channel to prevent particles and cells from settling in the tubing and device. Between experiments, devices are cleaned with filtered 2% tergazyme, filtered 10% bleach or piranha solution.

Data analysis. We first rescale the recorded frequency signals from each cantilever by applying a rough correction for the different sensitivities of the cantilevers. Cantilevers differing only in length should have mass sensitivities proportional to $f^{3/2}$. Therefore we initially divide each frequency signal by its carrier frequency to the power of 3/2 such that the signals are of similar magnitude. To detect peaks, we filter the data with a third-order Savitzky–Golay low-pass filter[39] followed by a nonlinear high-pass filter (subtracting the results of a moving quantile filter from the data). We find peak locations as local minima that occur below a user-defined threshold. After finding the peak locations, we estimate the peak heights by fitting the surrounding baseline signal (to account for a possible slope in the baseline that was not rejected by the high-pass filter), fitting the region surrounding the local minima with a fourth-order polynomial and finding the maximum difference between the predicted baseline and the local minima polynomial fit. Because this process occasionally makes errors (it sometimes detects noise, particles that got stuck in the cantilever and particles that passed through the cantilever at the same time), for each cantilever we reject peaks that are very unlike the typical peak. We do this by first calculating the robust Mahalanobis distance for each peak in terms of a number of its estimated characteristics (baseline slope, time between sequential antinode peaks, minimum value between sequential peaks and difference in heights of sequential peaks) and rejecting those with large distances above a user-specified threshold, then identifying the peaks corresponding to the calibration particles and precisely estimating the mass sensitivity for each cantilever such that the modal mass for the particles is equal to the expected modal mass according to the manufacturer's data sheet. Finally we match up peaks at different cantilevers that originate from the same cell to extract single-cell growth information (**Supplementary Note 3**). **Figures 2–5** show the mass accumulation rates of automatically matched cells that were observed at least seven times. For *E. coli* (**Fig. 6**), because the cell concentrations were higher, we required both that the cell was measured at least six out of ten times and that the r.m.s. error of a linear fit (buoyant mass versus time) was less than 5 fg, as a greater fitting error suggests a possibly incorrect matching.

Cell culture. *E. coli* strain 25922 (ATCC) was grown overnight in LB medium (Miller, Difco) at 37 °C. Saturated overnight cultures were diluted 10,000-fold in LB supplemented with 0.2% Tween-80 (to prevent particles from sticking to the device walls) and incubated 1.5–2.5 h in a shaker incubator at 37 °C before being loaded onto the serial SMR array. The CM15 peptide (sequence KWKLFKKIGAVLKVL; Biosynthesis) was ordered as a crude synthesis and suspended in water by weight. Kanamycin (Sigma-Aldrich) and CM15 were prepared as stock solutions at 50 mg/mL in water, and 1 μL of stock solution was added to 1 mL culture at the times indicated.

E. faecalis (ATCC strain 29212) was grown overnight in Brain Heart Infusion medium (BHI, Difco) at 37 °C. Saturated overnight cultures were diluted 100,000-fold in BHI with 0.2% Tween-80 and incubated for 3 h in a shaker incubator at 37 °C before being loaded onto the serial SMR array.

Yeast (strain W303, diploid) were a gift from A. Amon and were maintained on YPD agar plates and grown in YPD broth at 30 °C.

L1210 cells were a gift from M. Kirschner, and no further cell-line validation was performed. Ba/F3 cells expressing BCR and ABL were created[40] from the parental Ba/F3 cell line obtained from the RIKEN BioResource Center.

Both cell lines tested negative for mycoplasma. L1210 and Ba/F3 cells were cultured in filtered RPMI 1640 supplemented with 10% FBS and streptomycin and penicillin at 37 °C under 5% CO_2. Ba/F3 cells were cultured under identical conditions and were IL-3 independent owing to a BCR–ABL insertion.

Mouse CD8+ T cells were obtained from a 14-week-old female C57BL/6J mouse. Animals were cared for in accordance with federal, state, and local guidelines following a protocol approved by the Department of Comparative Medicine (DCM) at MIT. Cells were obtained from a mouse spleen and two lymph nodes, ground through a filter, subjected to ammonium–chloride–potassium (ACK) lysis, purified with a CD8a+ T Cell Isolation Kit (Miltenyi) and immediately seeded into wells and activated in RPMI 1640 with 10% FBS, 1× streptomycin–penicillin, and 55 μM β-mercaptoethanol (Gibco) using surface-bound anti-CD3 (BioLegend 145-2C11, coated at 5 μg/mL) and soluble anti-CD28 (BioLegend, 37.51, 2 μg/mL) at 37 °C under 5% CO_2 for 22 h. After 22 h, cells were transferred to new medium containing IL-2 (100 U/mL) and from then on were passaged daily to a concentration of roughly 200,000 cells/mL 2–3 h before each measurement.

Human blood buffy coat was obtained from Research Blood Components, and PBMCs were isolated with Ficoll-Paque Plus (GE) using the manufacturer's recommended protocol. The PBMC layer was isolated, subjected to ACK lysis (Thermo Fisher) and washed three times with RPMI 1640 supplemented with 10% FBS. Cells were then seeded in a 96-well plate (Corning High Bind microplate) at a concentration of 1.5×10^6 mL^{-1} with 5 μg/mL surface-bound anti-CD3 (BioLegend, HIT3a clone), 2 μg/mL soluble anti-CD28 (BioLegend, CD28.2 clone), and 100 U/mL soluble IL-2 (PeproTech) at 37 °C under 5% CO_2. Immediately before measurement, cells were harvested from the well by gentle pipetting to suspend weakly adhered cells, diluted into RPMI 1640 supplemented with 10% FBS and IL-2 and loaded into the serial SMR array.

All studies involving primary patient samples were approved by the Dana-Farber/Harvard Cancer Center Institutional Review Board. Informed consent was obtained in accordance with the Declaration of Helsinki. Diagnostic peripheral blood or bone marrow specimens were obtained from patients with acute myeloid leukemia (**Supplementary Table 1**), subject to erythrocyte lysis (Qiagen, #158904), and stained with antibodies targeting hCD45 (eBiosciences, #17-9459-42) and hCD15 (eBiosciences, #12-0159-42). Leukemia cells were enriched by sorting for hCD45+hCD15+ (double-positive) cells on a FACSAria II SORP fluorescence activated cell sorter (BD Biosciences) (**Supplementary Fig. 8**). Sorted cells were seeded at a density of 1×10^6 cells/mL and cultured at 37 °C in a humidified 5% CO_2 incubator in RPMI (Gibco) supplemented with 10% FCS (Gibco), 2 mM L-glutamine (Gibco), and 50 IU/ml–50 μg/mL penicillin–streptomycin (Fisher Scientific) before dilution and loading on the SMR.

36. Burg, T.P. *et al.* Weighing of biomolecules, single cells and single nanoparticles in fluid. *Nature* **446**, 1066–1069 (2007).
37. Olcum, S. *et al.* Weighing nanoparticles in solution at the attogram scale. *Proc. Natl. Acad. Sci. USA* **111**, 1310–1315 (2014).
38. Stone, H.A. in *CMOS Biotechnology* (eds. Lee, H., Westervelt, R.M. & Ham, D.) 5–30 (Springer US, 2007).
39. Savitzky, A. & Golay, M.J.E. Smoothing and differentiation of data by simplified least squares procedures. *Anal. Chem.* **36**, 1627–1639 (1964).
40. Lane, A.A. *et al.* Triplication of a 21q22 region contributes to B cell transformation through HMGN1 overexpression and loss of histone H3 Lys27 trimethylation. *Nat. Genet.* **46**, 618–623 (2014).
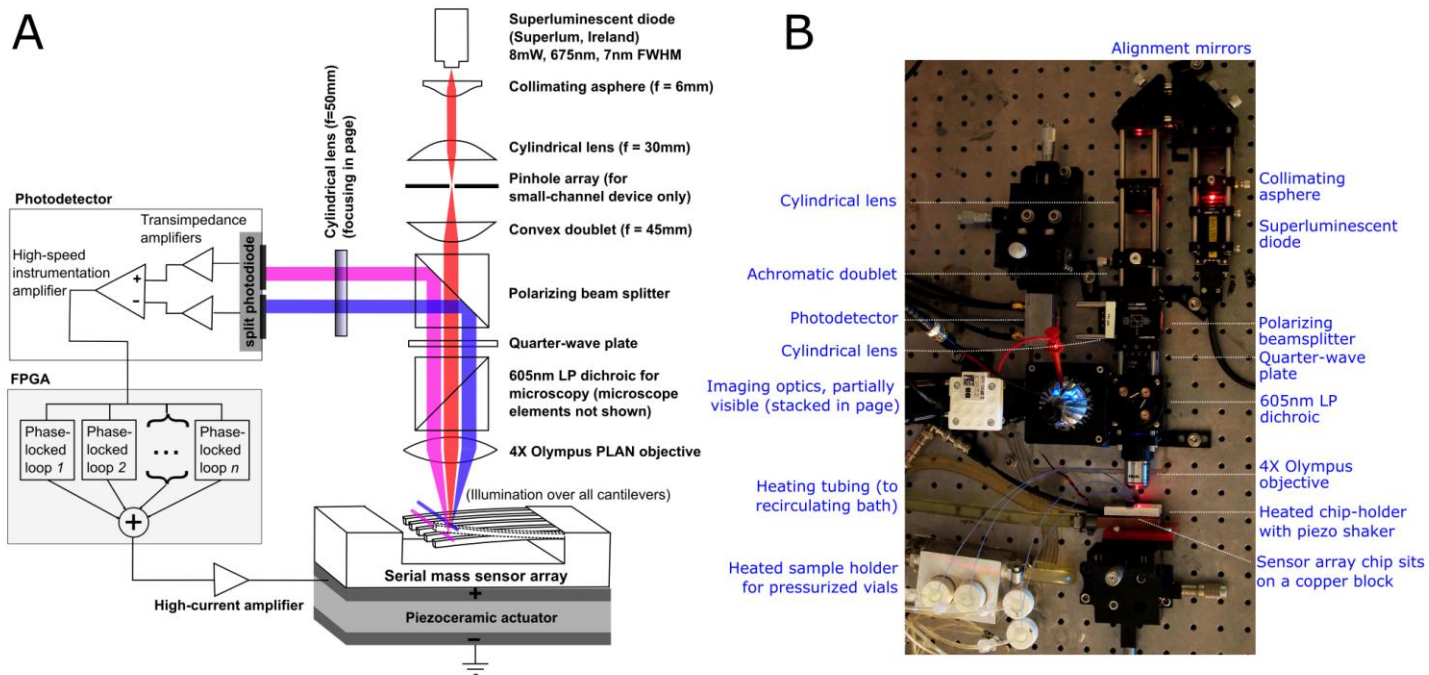
Supplementary Figure 1

Schematic of the control system for the serial microfluidic mass sensor array.

(A) Schematic of optical and electronic path of parallel feedback loops for each mass sensor. (B) Photograph of the optical setup implementing the schematic in (A). The photograph shows the sample holder and the fluidic connections to the sensor chip.
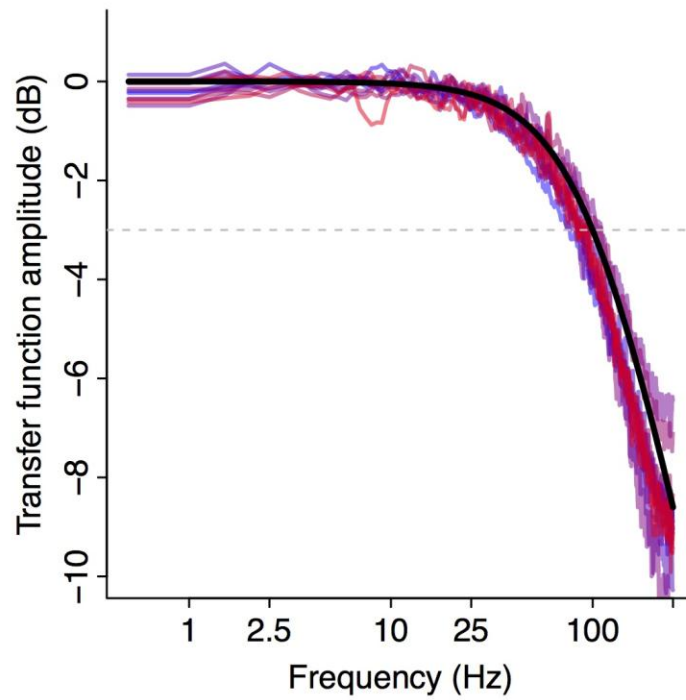
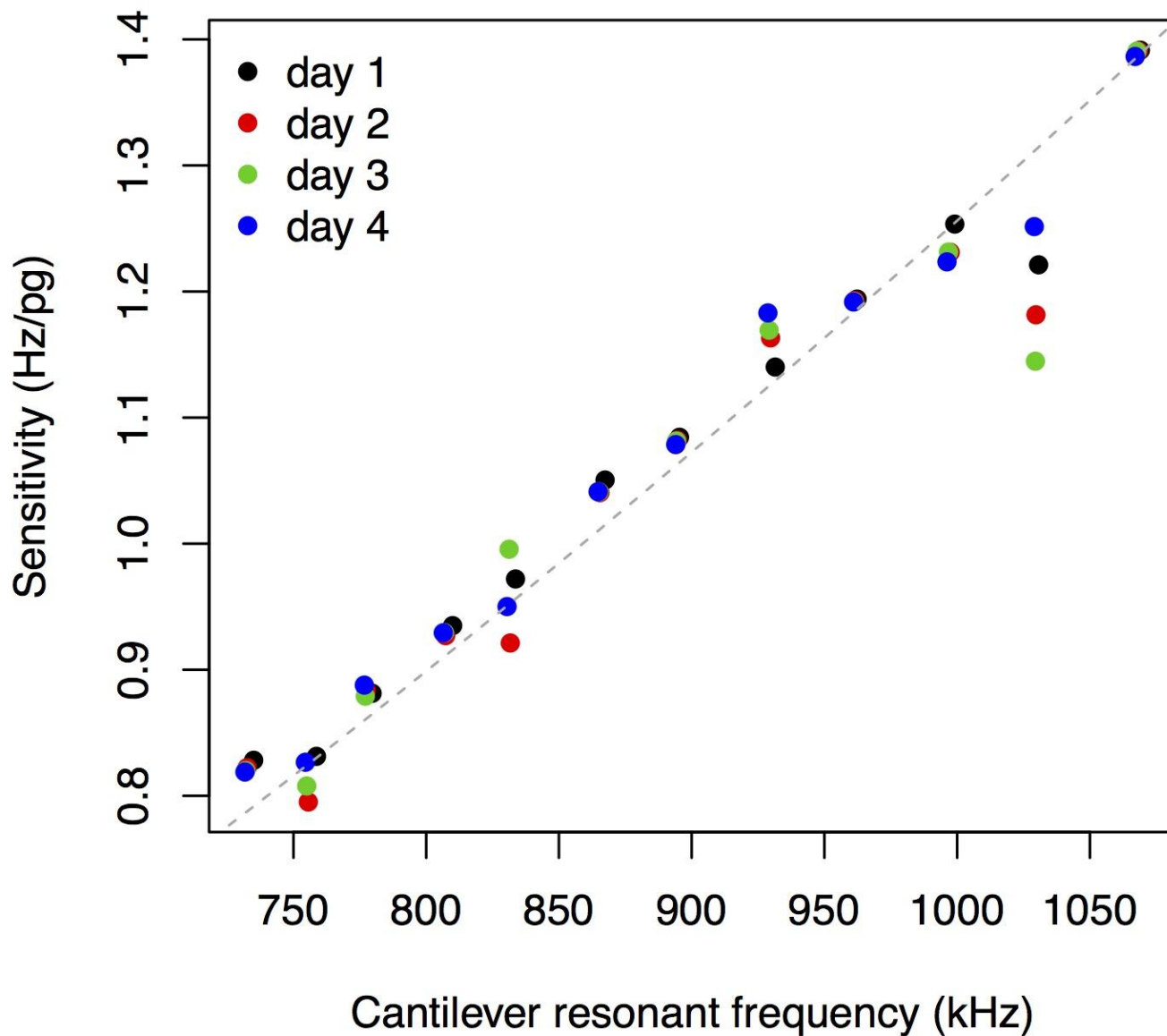**Supplementary Figure 2**

Transfer functions of the PLL–cantilever control loops.

Measured transfer functions (colored lines) of all twelve PLL-cantilever feedback loops on a single large-channel serial SMR device. Bandwidth had been set to 100 Hz according to the method in [1]. Solid black line shows ideal 100 Hz first-order response, dashed grey line indicates -3 dB bandwidth.

Supplementary Figure 3

Sensitivities of the mass sensors in a large-channel device.

Resonant frequency versus mass sensitivity for a single large-channel device, measured daily during the mouse CD8 cell experiments (Figure 3 in the main text). Dashed grey line shows best fit of data to $y = ax^{1.5}$, illustrating how sensitivity scales with frequency to the power of 1.5. While fabrication tolerances and slight variations in geometry may explain some of the deviations from the model, it remains unclear why some cantilevers exhibit substantial day-to-day variation.
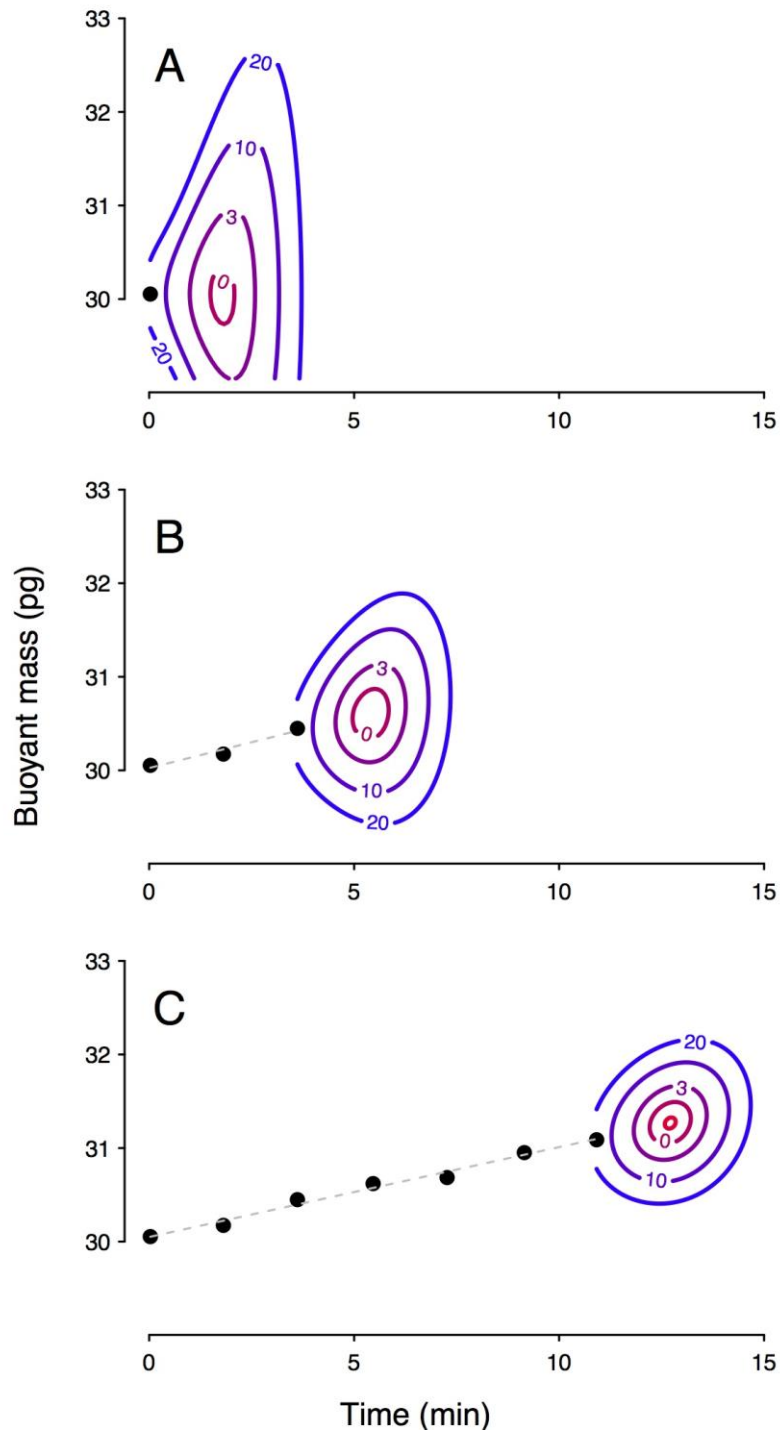
Supplementary Figure 4

Example contour plots of the cost function used in the matching algorithm.

Contour plots of the cost function for several simulated example cells with varying numbers of previous peaks observed (black points). (A) If a cell only has a single peak assigned, the cost function is shaped like a wide bowl, shaped almost entirely by the prior assumptions on mass accumulation rate and system noise. (B), (C) As more data points are observed, the mass accumulation rate becomes established and the cost function contours become determined by the system's mass measurement noise.
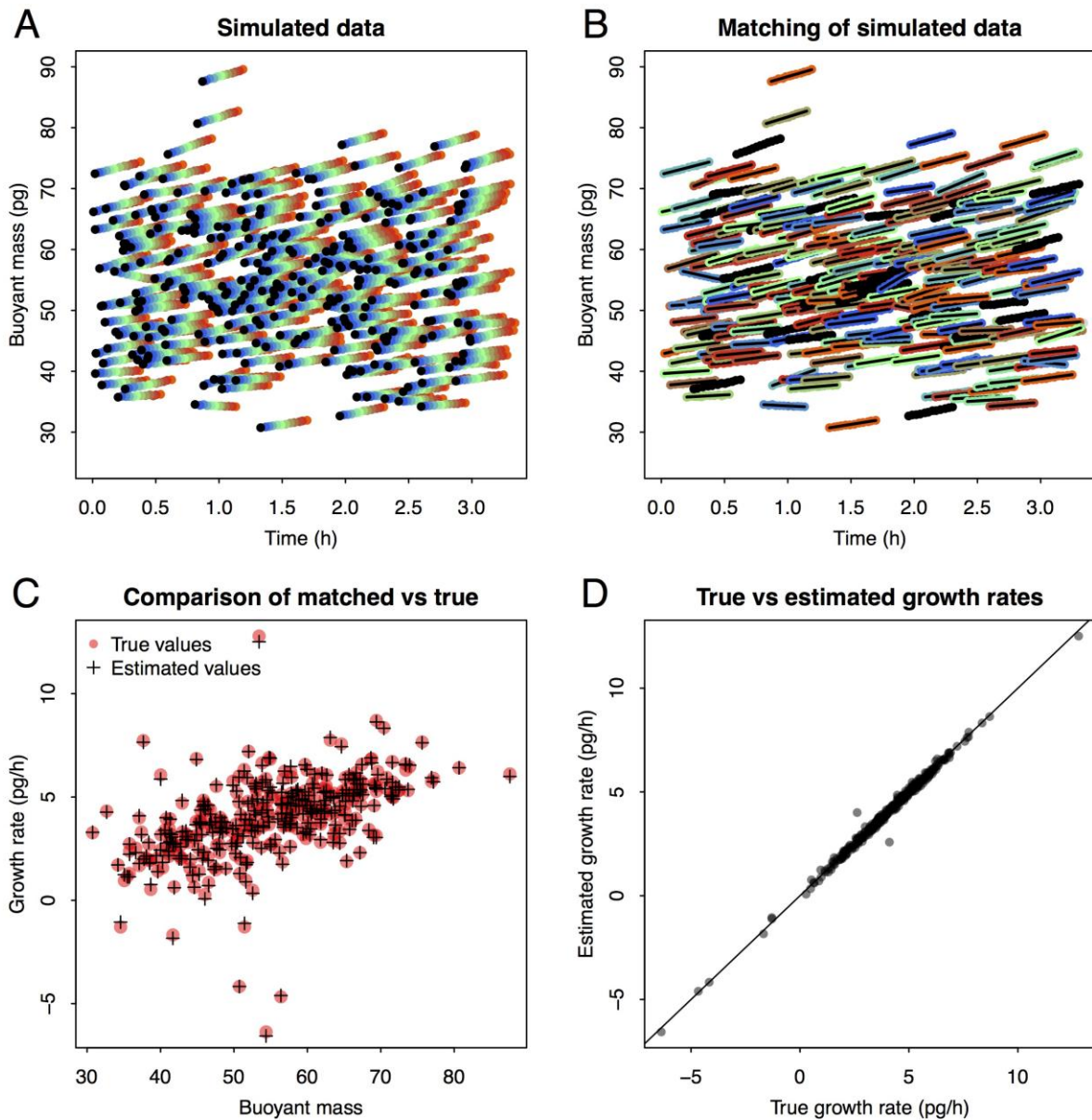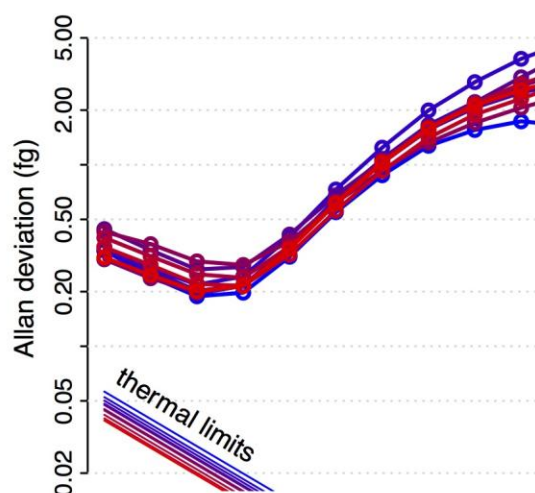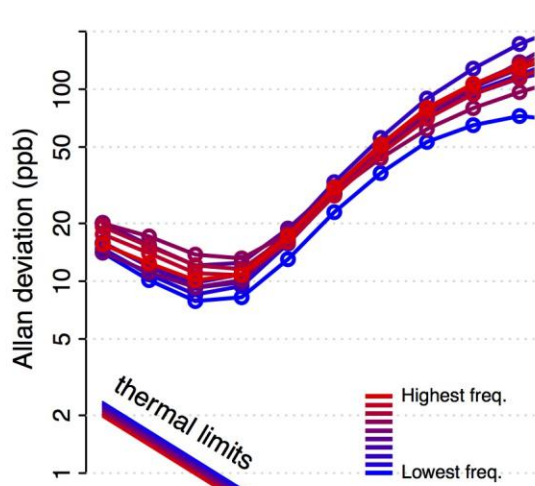
Supplementary Figure 5

Simulation of the cell-matching process.

Simulation of the cell matching process showing that single cells are reliably matched by our method. (A) We simulate a set of cells sampled from a joint distribution of mass and mass accumulation rate similar to the L1210 cells shown in Figure 2. However, we simulate cells entering the serial SMR array at a rate of 100 cells per hour (two-fold more concentrated than we have used in our experiments). Each cell varies in the time it takes to travel from each cantilever to the next (mean 1.9 minutes, standard deviation 0.3 minutes), and Gaussian noise is added to each buoyant mass measurement (standard deviation 0.05 pg, similar to that of our large-channel device). (B) We then match the measurements in the simulated data. All data points that have been matched together as corresponding to the same cell have been colored the same randomly-chosen color. (C) Comparison of the masses and mass accumulation rates from which the data in (A) was generated, and the observed mass and mass accumulation rates, showing excellent agreement. (D) Comparison of mass accumulation rates from which the data in (A) was generated, and the observed mass accumulation rates, showing excellent agreement, except for in the case of two mismatched cells (off-diagonal points) out of 300 in the simulated dataset.
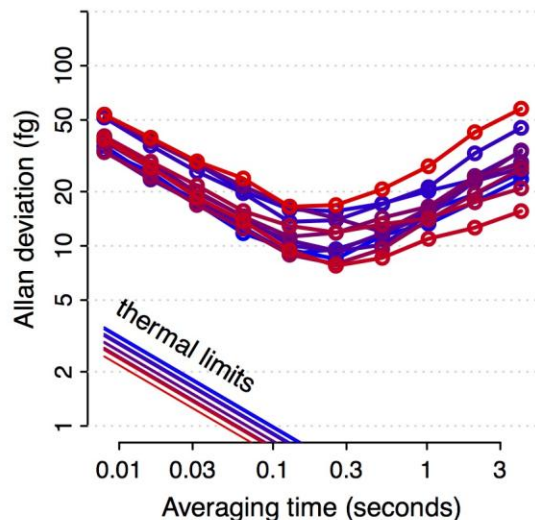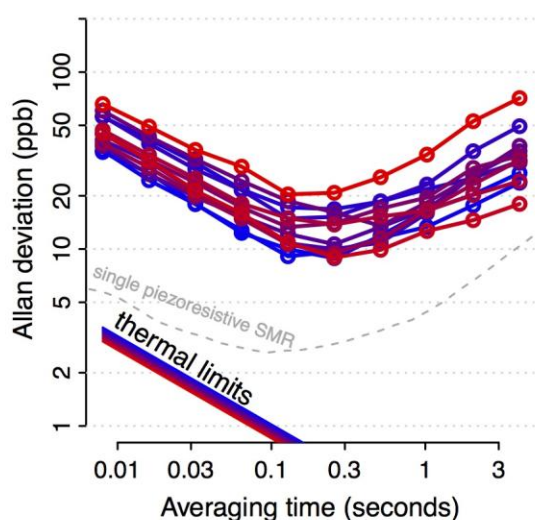
Supplementary Figure 6

Stability of the cantilevers used in the mass sensor arrays.

Measured Allan deviations of all cantilevers on two separate devices. Left two plots show Allan deviations in fractional frequency units, relative to the unloaded cantilever frequency (colored dots/lines). For reference, the dashed grey line indicates the measured noise performance of an optimized piezoresistive single large-channel SMR. Right two plots show Allan deviations rescaled by each cantilever's mass sensitivity. Theoretical thermomechanical limitations on the lowest achievable Allan deviations are also plotted (calculated from [2]), assuming the cantilever is driven to a mean-squared displacement one billion times (90 dB) above the thermally-driven mean-squared displacement. While larger drive amplitudes would theoretically further reduce these limits, mechanical nonlinearity typically becomes significant beyond 90 dB, limiting noise performance.
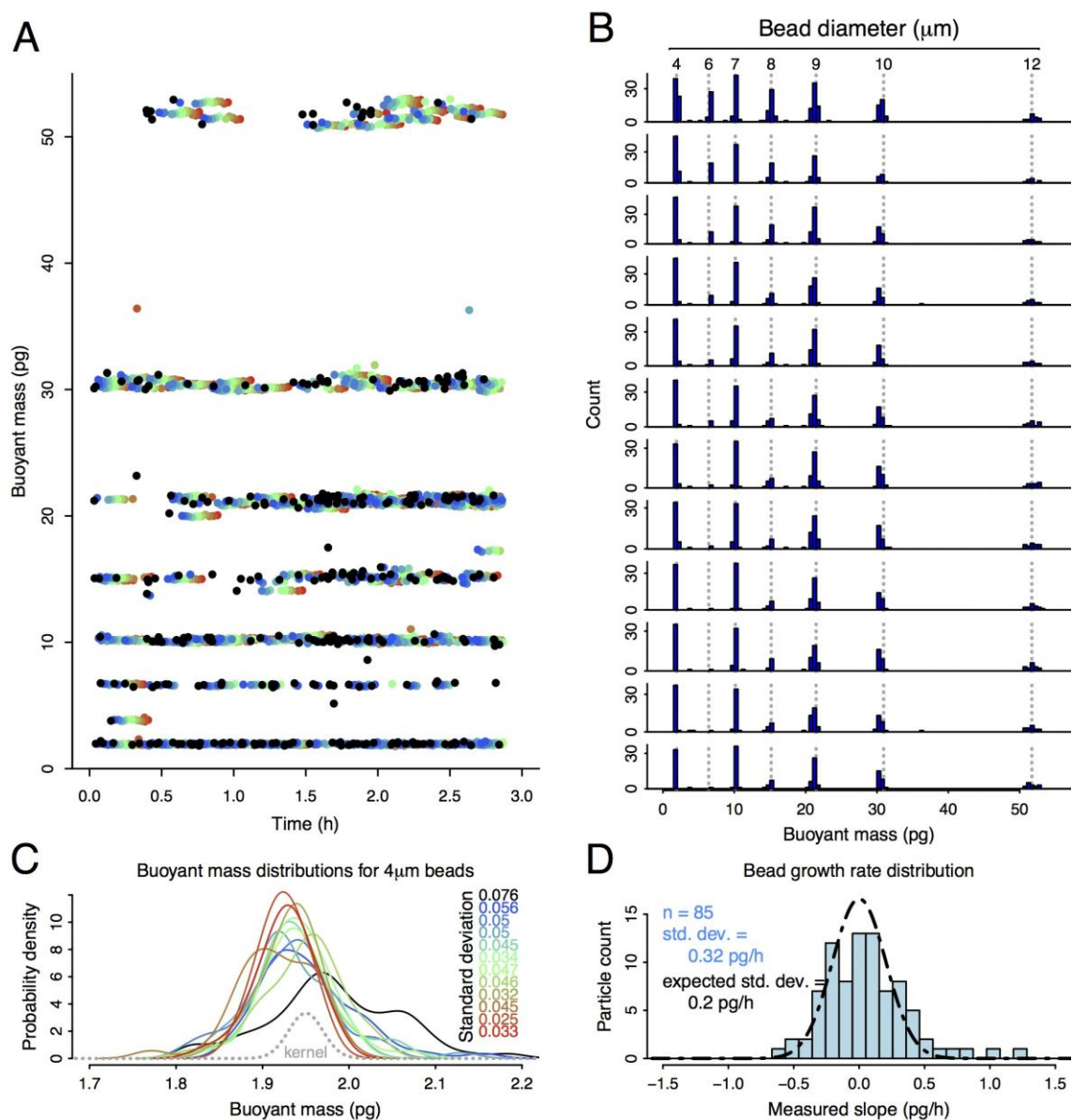
Supplementary Figure 7

Mass accumulation rate resolution of the large-channel devices.

Measuring a mixture of plastic microparticles to determine mass accumulation rate resolution on a large-channel serial mass sensor array. (A) We measured a mixture of 4, 6, 7, 8, 9, 10 and 12 μm polystyrene beads (Duke Standards, NIST traceable, Thermo Scientific) at 37 C in 0.01% Tween-20 in water. Sensors were calibrated by linearly rescaling their raw frequency signals such that the 7 μm bead modal mass is the expected buoyant mass (10.15 pg). (B) Across all sizes and sensors, particle buoyant masses match the expected buoyant masses (dashed lines), verifying that the sensors are linear over this size range. (C) 4 μm particles have the lowest size variability (in pg) of these beads according to manufacturer's datasheet, and therefore their distribution's width is a reasonable upper bound on the sensor error. Typical sensor root-mean-square-error is on the order of 0.05 pg. (D) Histogram of mass accumulation rates (errors, as particles are not growing) of 85 single particles for which at least 10 sensors could be linked together. Mass accumulation rates were calculated excluding data from the first sensor, which displayed much higher noise than the other sensors. Dashed line shows estimated mass accumulation rate distribution assuming t = 1.4 minutes, k = 11, and σ = 0.05 pg, showing good agreement between this approximation for mass accumulation rate error and the observed mass accumulation rate error distribution.
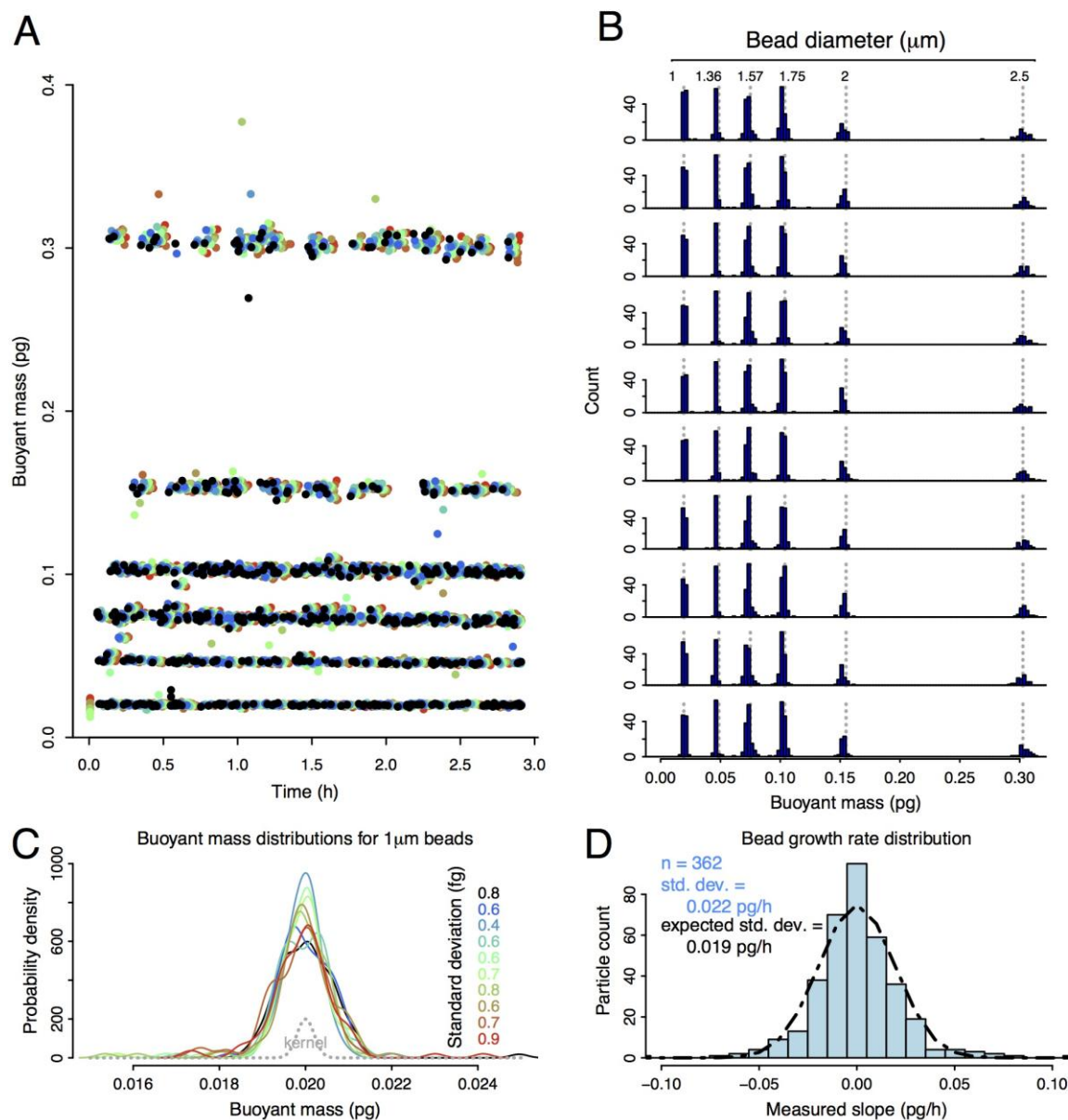
Supplementary Figure 8

Mass accumulation rate resolution of the small-channel devices.

Same as Supplementary Figure 7, but for a small-channel serial SMR array. (A) We measured a mixture of 1.0, 1.36, 1.57, 1.74, 2.0, and 2.5 μm polystyrene beads (Duke Standards, Thermo Scientific, except for 1.0 μm, from Bangs Labs) at 37 C in LB with 0.1% Tween-80. Sensors were calibrated by linearly rescaling their raw frequency signals such that the 1.0 μm bead modal buoyant mass is 0.02 pg (the expected buoyant mass in LB at a density of 1.013 g/mL). (B) Distributions of measured buoyant masses for each SMR in the array, demonstrating both linearity and precision in each cantilever mass measurement. (C) Buoyant mass distributions of 1 μm polystyrene particles provide an upper bound on each cantilever's buoyant mass measurement error, here on the order of 0.5-1 fg. (D) Mass accumulation rate distribution of single 362 single particles, yielding a mass accumulation rate standard error of 0.022 pg/h. Dashed line shows mass accumulation rate distribution based on equation 2 assuming t = 24 seconds, k = 10, and σ = 0.001 pg.
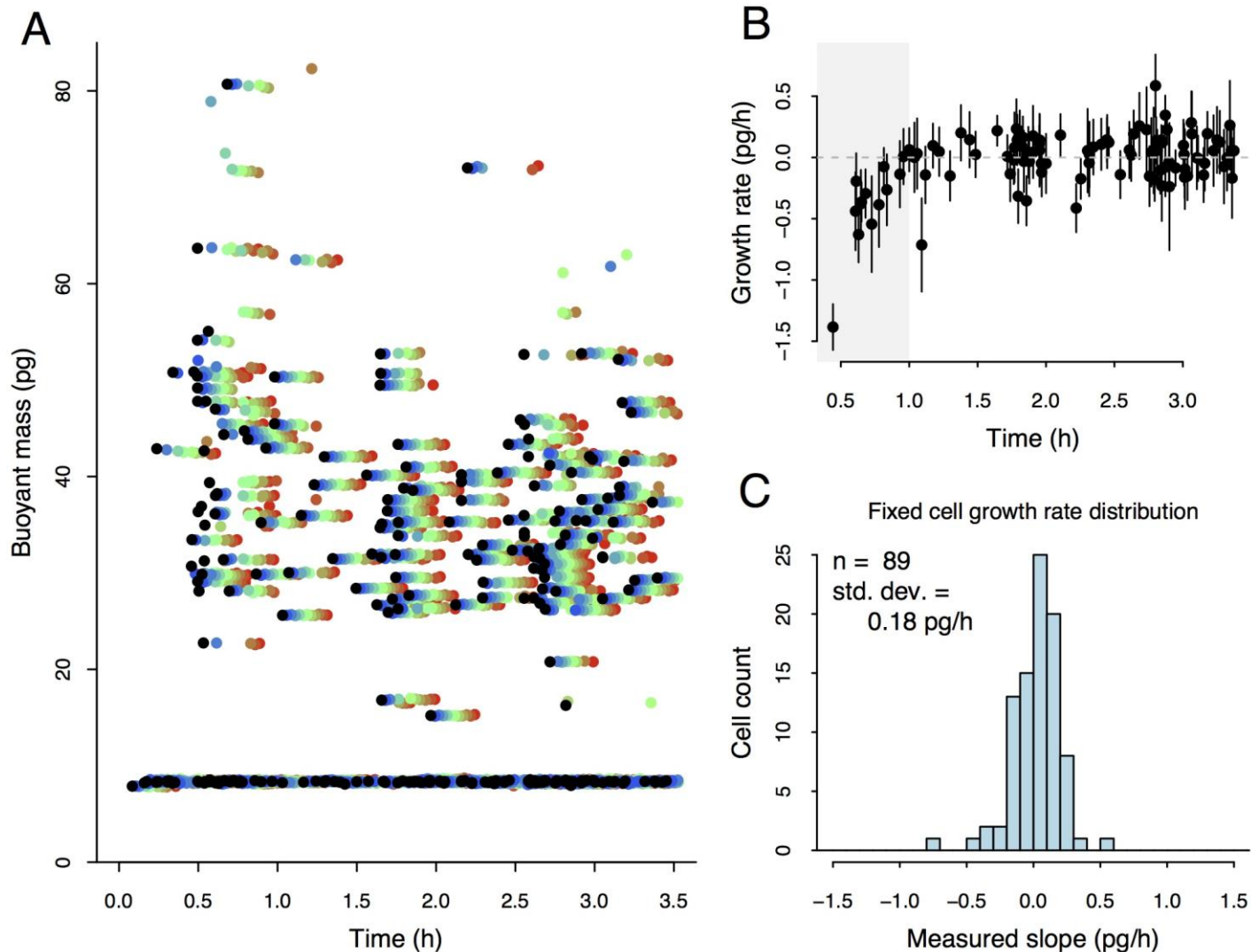
Supplementary Figure 9

Mass accumulation rate of a fixed mouse lymphoblast cell line (L1210).

(A) Buoyant mass trajectories for fixed L1210 cells, measured in phosphate-buffered saline at 37 C. (B) By plotting mass accumulation rate against time, the first cells going through the array can be seen to be losing mass. We believe this is real mass loss attributable to the temperature shift (cells had been fixed and stored at 4 C), and note that after one hour into the measurement cells appear to have equilibrated and no further mass loss occurs. (C) Histogram of mass accumulation rates of fixed cells, excluding the first hour of measurements.
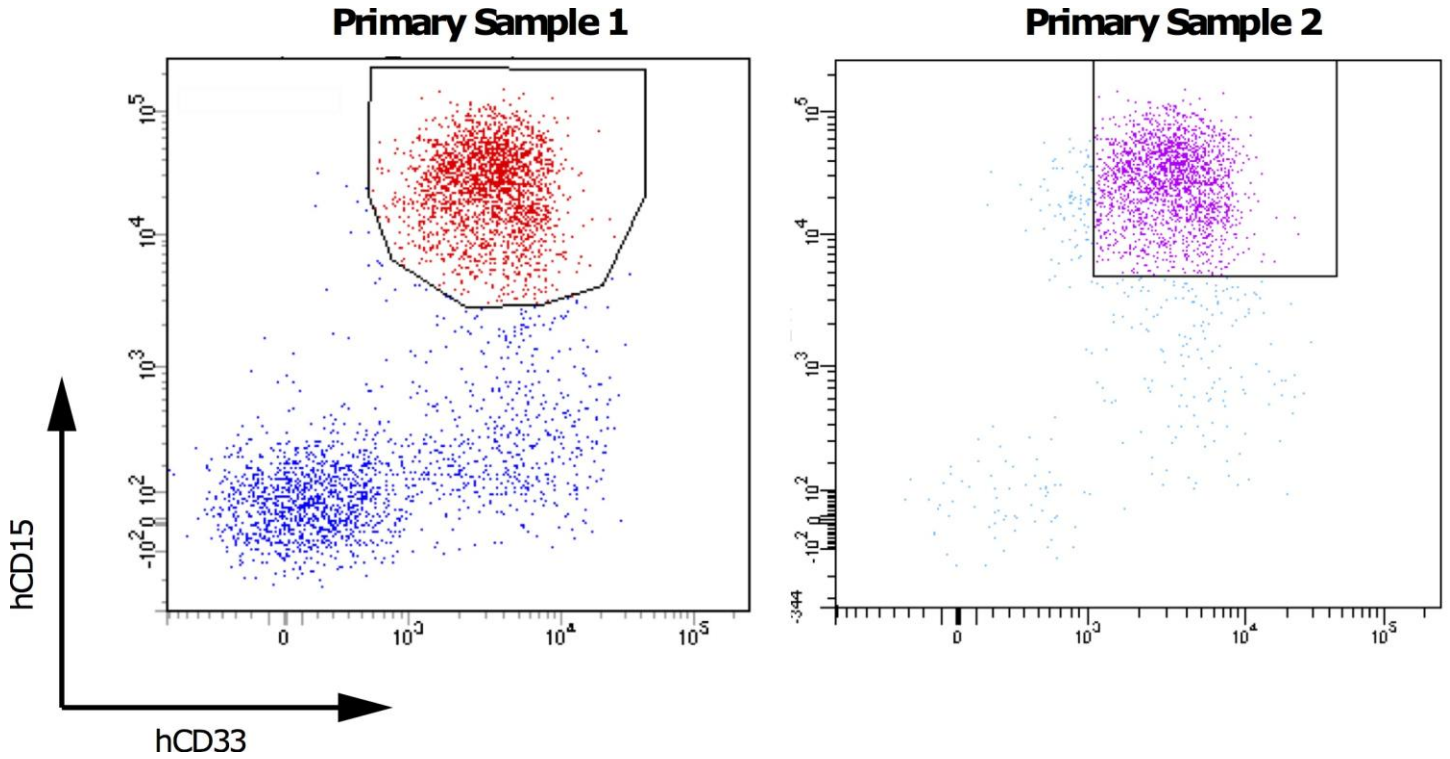
Supplementary Figure 10

FACS plots of primary acute myeloid leukemia cells.

FACS plots of two primary AML samples whose growth properties were assessed on the SMR. Fresh primary peripheral blood or bone marrow samples from patients with newly diagnosed AML were subject to erythrocyte lysis and stained with antibodies targeting human CD33 and human CD15, and leukemia cells were enriched by performing FACS for hCD33/hCD15 double-positive cells. Left panel (sample 1): primary peripheral blood sample from a patient with AML with monocytic differentiation and extensive circulating disease. Contemporaneous clinical testing confirmed that this leukemia expressed CD33 and CD15 and demonstrated that it comprised 43% of peripheral blood mononuclear cells, on which this sample was gated. Of note, this specimen was obtained after the patient had received cytoreductive chemotherapy (hydroxyurea) for three days. Right panel (sample 2): primary bone marrow aspirate from a patient with therapy-related AML. Of note, this specimen did not undergo immunophenotyping by the clinical lab, but morphologic analysis suggested that the leukemia comprised a minority of cells in this double-positive population.
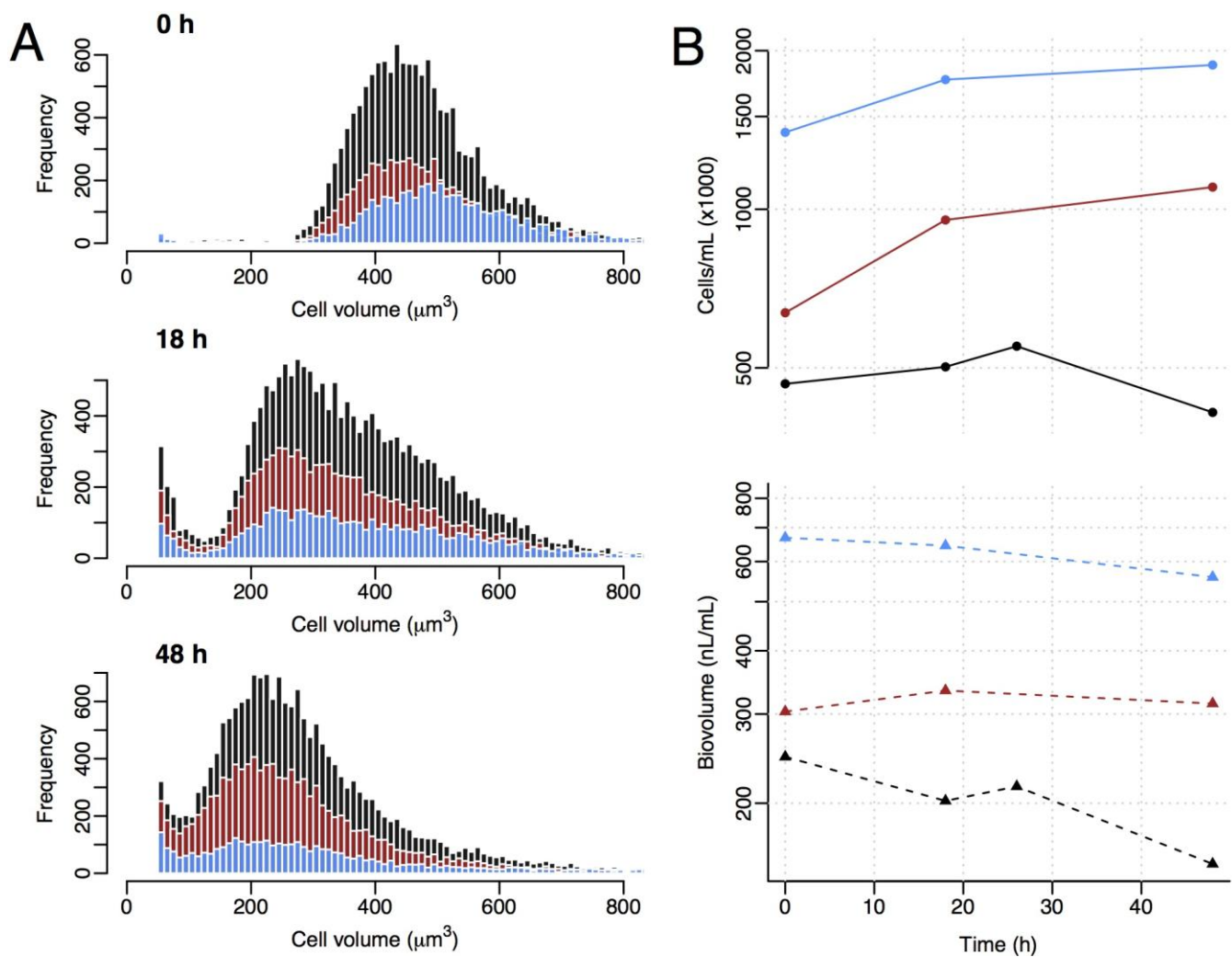
Supplementary Figure 11

Culturing AML cells *ex vivo*.

We seeded cells obtained from Patient 1 (Figure 4 and Supplementary Figure 10) at 0.5, 0.7 and 1.5 million cells/mL (blue, red, and black, respectively) into 6-well culture dishes. (A) We profiled these cultures volume distributions over the next 48 hours with a coulter counter (Beckman Coulter Multisizer 4, 100 μm aperture). The cultures behaved similarly for different inoculation densities. (B) Total cell counts generally increased slightly, but total biovolume decreased.
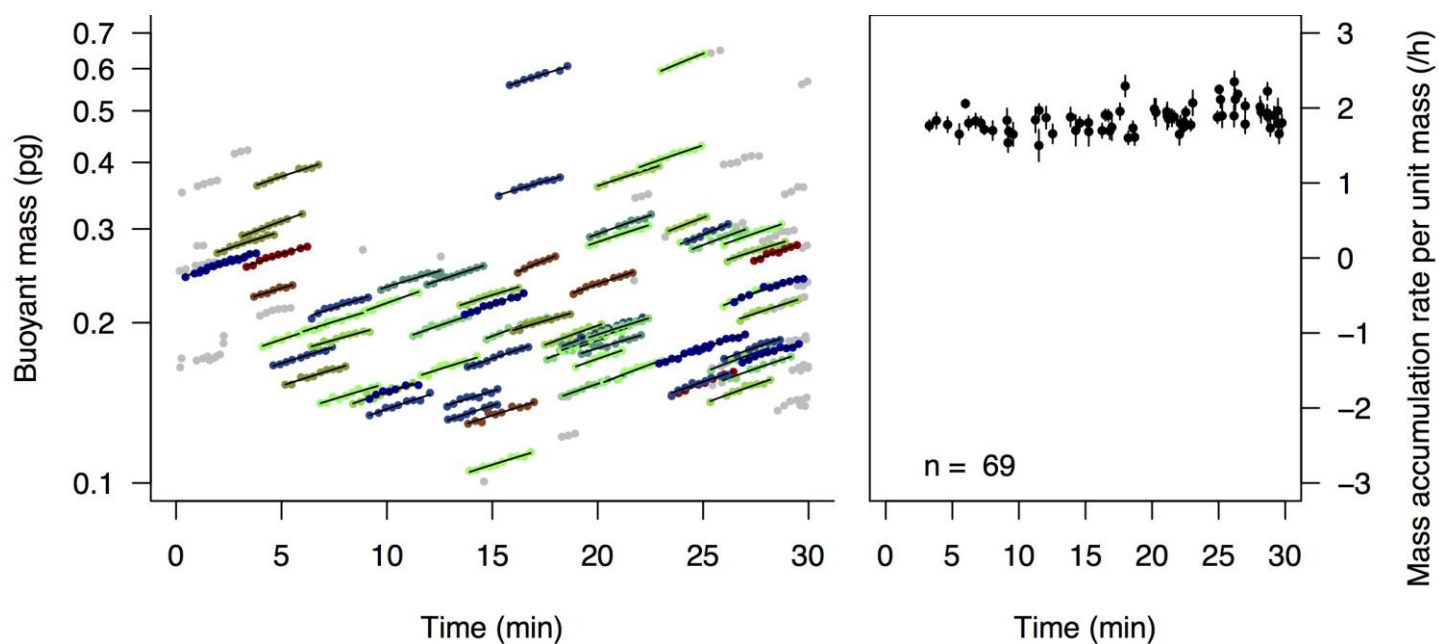
Supplementary Figure 12

Mass accumulation rate of *E. faecalis* measured on a small-channel mass sensor array.

At the left, colored dots show points which were determined to correspond to a single cell, for which the mass accumulation rate was determined and plotted against the cell's mass (right). Grey points indicate measurements for which less than seven mass measurements could be linked together, and were not used in the analysis at right. E. faecalis was grown in Brain-Heart Infusion (BHI, Difco) overnight and transferred to fresh BHI with 0.2% Tween-80 at a 105-fold dilution approximately three hours prior to measurement. 1.36 μm beads were used as the calibration standard and have been omitted from the plot at left for clarity.
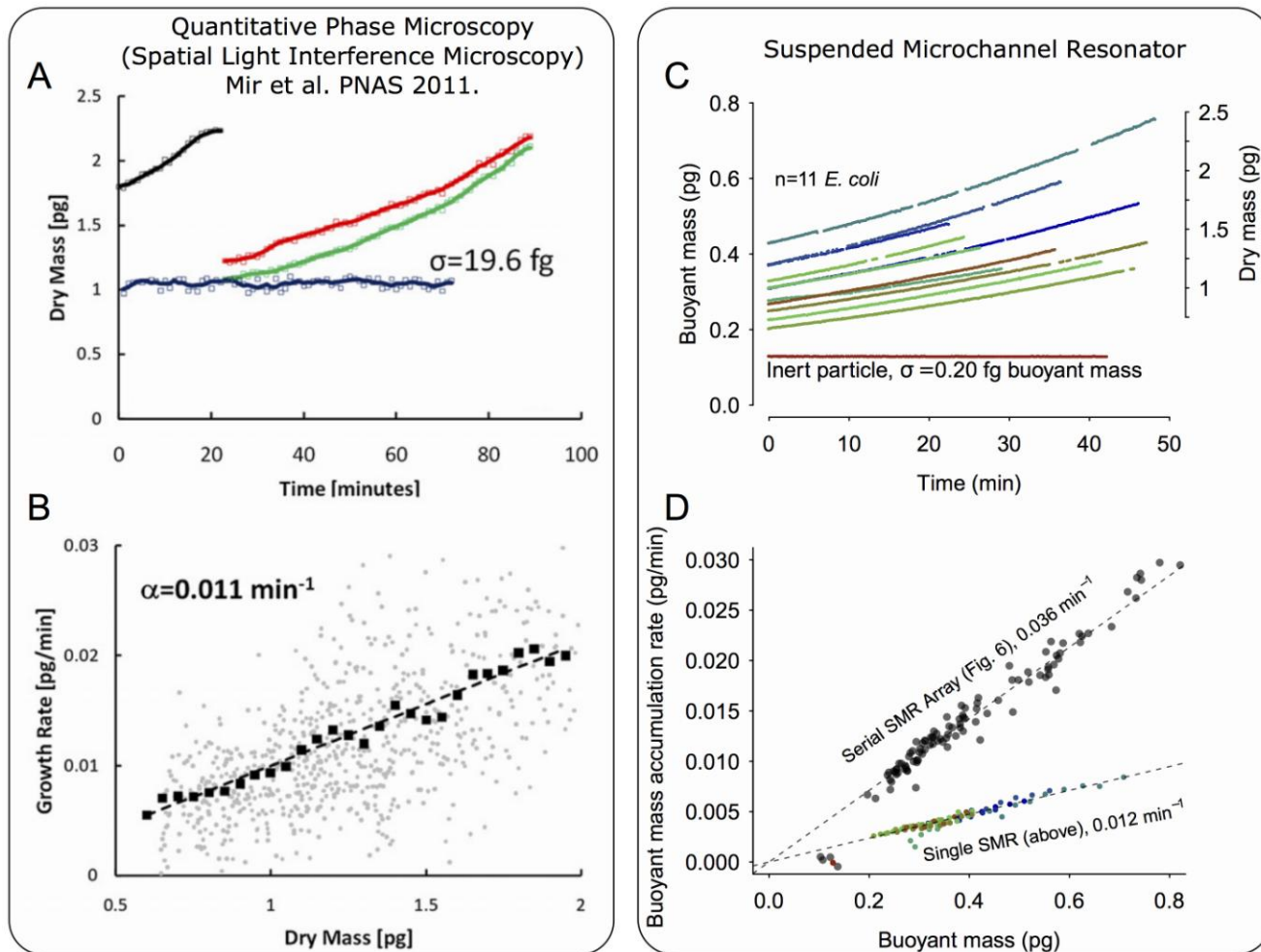
Supplementary Figure 13

Comparison of precision between recent quantitative-phase microscopy measurements and SMR measurements.

Plots in (A) and (B) are excerpted from Mir et al. [3]. Insets in the original figure (A) and caption segment describing the insets have been omitted for clarity. Original caption reads:

> SLIM measurements of E. coli growth. (A) Dry mass vs. time for a cell family. [...] The blue line is a fixed cell measurement, with SD of 19.6 fg. Markers indicate raw data, and solid lines indicate averaged data. (B) Growth rate vs. mass of 20 cells measured in the same manner. Faint circles indicate single data points from individual cell growth curves, dark squares show the average, and the dashed line is a linear fit through the averaged data; the slope of this line, 0.011 min 1, is a measure of the average growth constant for this population. The linear relationship between the growth rate and mass indicates that, on average, E. coli cells exhibit exponential growth behavior.

(C) Single-cell E. coli (ATCC 43893) growth trajectories measured on a single SMR (160 μm long with a 3 by 5 μm interior channel, operated in the second vibrational mode at 1.1 MHz) of similar design to the SMRs in serial SMR arrays. Growth was measured by passing a single cell back and forth through the SMR, as in [4]. Data points from other cells that entered the sensor during the dynamic trap (but were ignored by the trapping algorithm) were removed. SMR measurements were made in LB at room temperature, yielding a similar growth rate as in Mir et al. [3], which used E. coli MG1655 in M9-casamino acid media at 37 C. (D) Colored points are buoyant mass accumulation rates estimated from the data in (C), based on linear fits to non-overlapping 5-minute segments. Five minutes was chosen as that was the width of the applied smoothing filter in (A) and (B). Black points are mass accumulation rates from *E. coli* cells at 37 C measured in the serial SMR array in Figure 6A. Dashed lines show best linear fits in which the intercept was forced to zero, and corresponding exponential growth rates are noted for the two experiments. Note that the terminology of 'growth rate' used in (B) is equivalent to 'mass accumulation rate'.
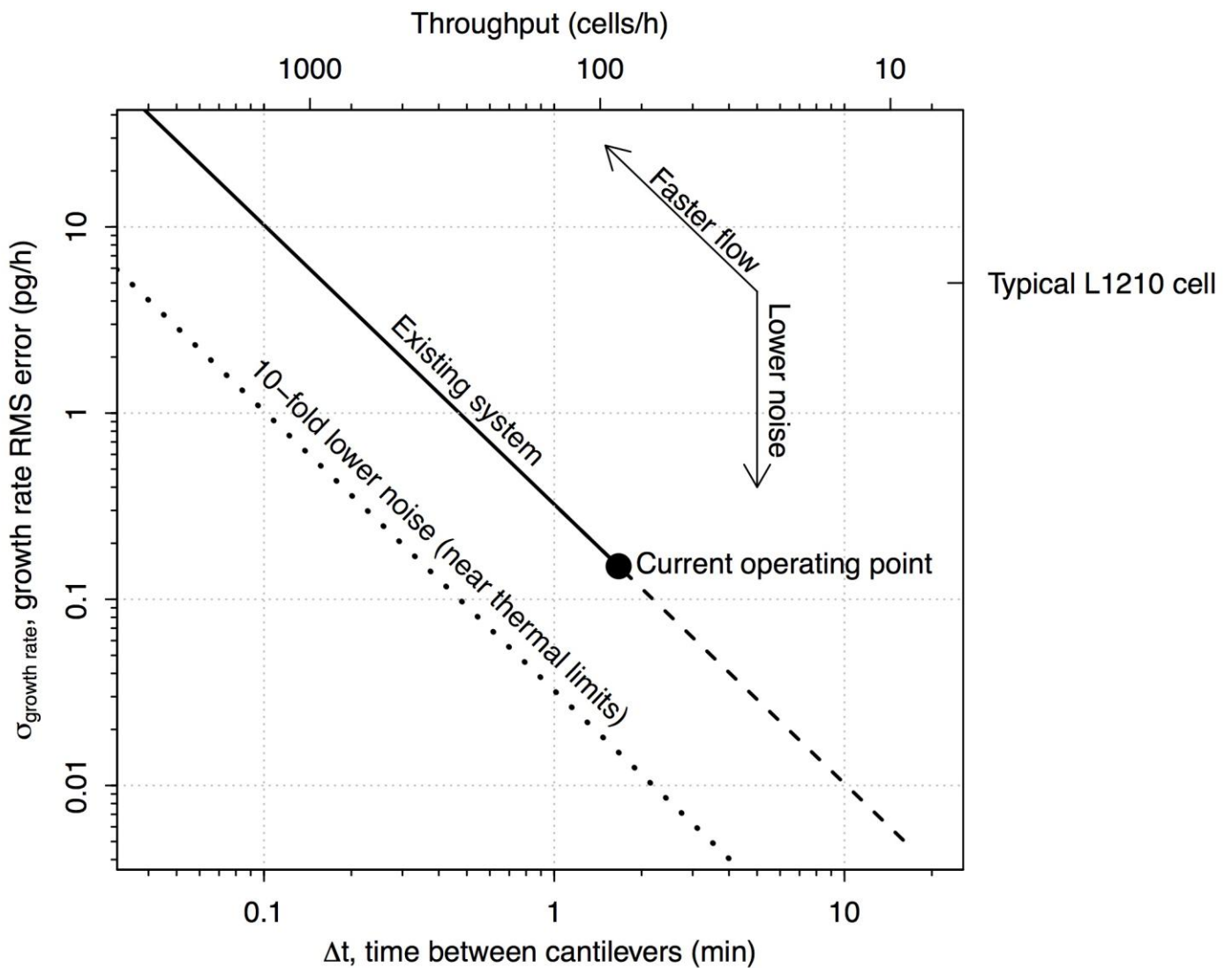
Supplementary Figure 14

Theoretical trade-off between throughput and resolution.

Theoretical trade-off between throughput and resolution for the large-channel devices used in this study, with 12 mass sensors and delay channels with volumes 120-fold higher than the volume of a single cantilever. We assume the cell concentration cannot exceed one cell per 50 sensor volumes (to avoid two cells being in the sensor at the same time), yielding the line of possible operating points.
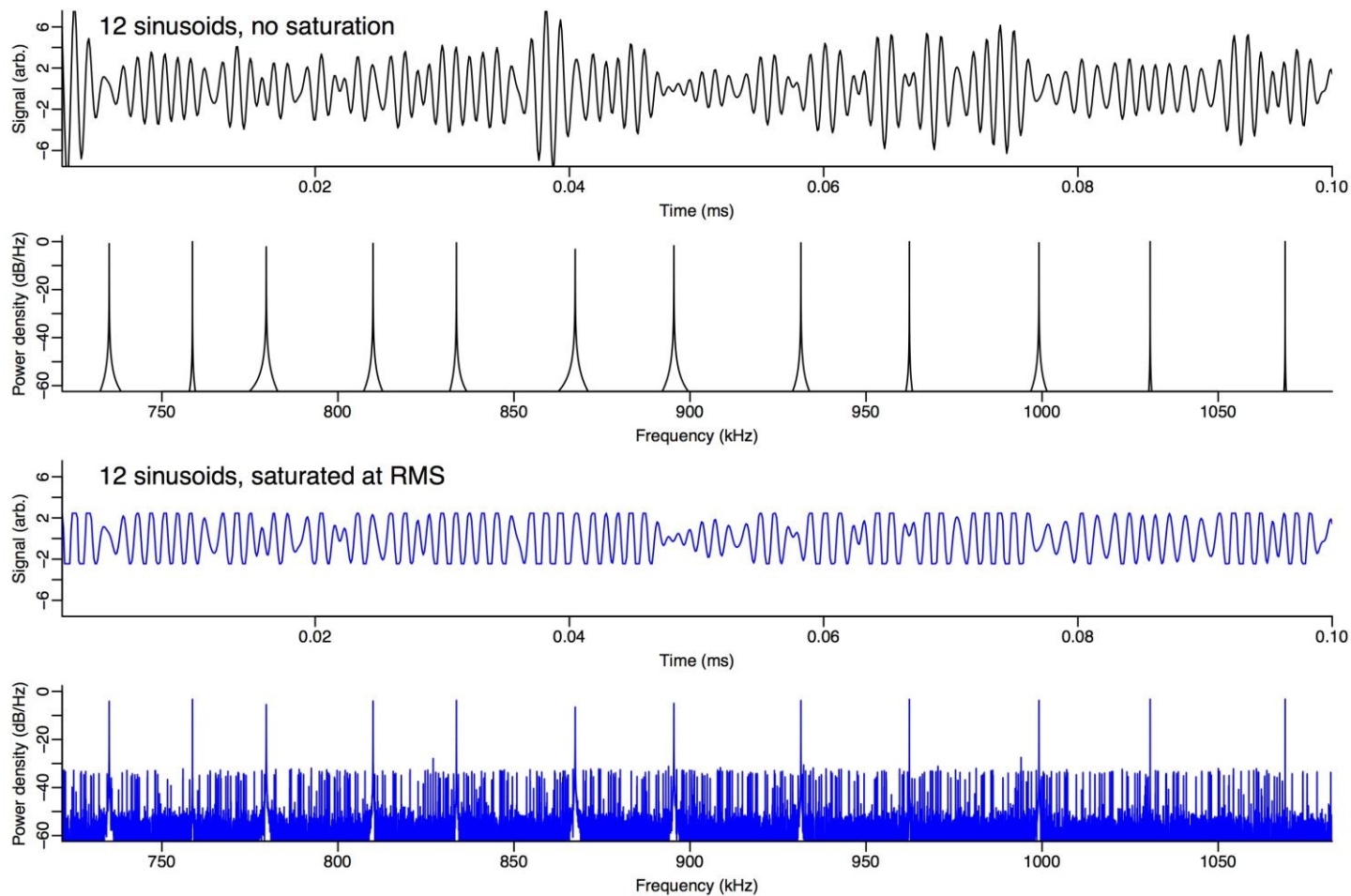
Supplementary Figure 15

Effect of signal clipping in power spectral density around the sensor resonant frequencies.

Saturation applied to a channel carrying many sinusoids adds many other spectral components that are not easily filtered out (noise).

	Primary Sample 1	Primary Sample 2
Patient Characteristics		
Age	82	62
Gender	Male	Female
Tumor Characteristics		
Diagnosis	AML with monocytic differentiation	AML (therapy-related)
Diagnostic tissue	Peripheral blood	Bone marrow
Involvement by Leukemia (%)	43	6
Immunophenotype		
Positive	CD45 (dim), HLA-DR, CD56 (subset), CD13, CD33, CD15, CD14 (variable), CD11b (subset), CD64	N/A
Negative	CD34, CD117	N/A
Karyotype	Normal (46,XY)	46,XX, t(1;16)(p32;p13.1), t(8;21)(q22;q22)
Molecular abnormalities	FLT3, NPM1, TET2 mutations	None detected
Prior AML therapy	Hydroxyurea x 3 days	None

Supplementary Table 1

Clinical characteristics of primary AML samples studied with a serial SMR array.

Note 1: Resolution of mass accumulation rate sensor

How precisely can we measure the mass accumulation rate of a cell? To measure the mass accumulation rate, we will measure the cell size k times, once every Δt minutes, and fit a model to explain how it varies over time. Here we will assume the total duration of the measurements ($k\Delta t$) is short enough that a line is an appropriate model. So the problem becomes, how precisely can we know the slope of a line?

Fortunately, least-squares slope estimates can be written as a linear combination of the observed size values, Y, as follows [5]:

$$\begin{bmatrix} \text{intercept} \\ \text{slope} \end{bmatrix} = (X^T X)^{-1} X^T Y$$

Here X is a $k \times 2$ matrix, where the first column is filled with ones, and the second column corresponds to the evenly-spaced times at which the cell size is measured. For simplicity, we assume the times are mean-centered, yielding the following time vector:

$$\begin{bmatrix} \frac{-k+1}{2}\Delta t & \frac{-k+3}{2}\Delta t & \frac{-k+5}{2}\Delta t & \dots & \frac{k-1}{2}\Delta t \end{bmatrix}$$

which we will generally simply denote as $\begin{bmatrix} \frac{-k+1}{2}\Delta t & \dots & \frac{k-1}{2}\Delta t \end{bmatrix}$. Plugging in this definition of X gets us to the coefficient vector relating the measured sizes to the slope estimator (specifically, this coefficient vector is the second row of $(X^T X)^{-1} X^T$).

$$\begin{bmatrix} \text{intercept} \\ \text{slope} \end{bmatrix} = \left(\begin{bmatrix} 1 & \dots & 1 \\ \frac{-k+1}{2}\Delta t & \dots & \frac{k-1}{2}\Delta t \end{bmatrix} \begin{bmatrix} 1 & \frac{-k+1}{2}\Delta t \\ \vdots & \vdots \\ 1 & \frac{k-1}{2}\Delta t \end{bmatrix} \right)^{-1} \begin{bmatrix} 1 & \dots & 1 \\ \frac{-k+1}{2}\Delta t & \dots & \frac{k-1}{2}\Delta t \end{bmatrix} \begin{bmatrix} y_1 \\ \vdots \\ y_k \end{bmatrix} \quad (1)$$

$$\begin{bmatrix} \text{intercept} \\ \text{slope} \end{bmatrix} = \left(\begin{bmatrix} k & 0 \\ 0 & \Delta t^2 \frac{k^3-k}{12} \end{bmatrix} \right)^{-1} \begin{bmatrix} 1 & \dots & 1 \\ \frac{-k+1}{2}\Delta t & \dots & \frac{k-1}{2}\Delta t \end{bmatrix} \begin{bmatrix} y_1 \\ \vdots \\ y_k \end{bmatrix}$$

$$\begin{bmatrix} \text{intercept} \\ \text{slope} \end{bmatrix} = \frac{1}{k\Delta t^2 \frac{k^3-k}{12}} \begin{bmatrix} \Delta t^2 \frac{k^3-k}{12} & 0 \\ 0 & k \end{bmatrix} \begin{bmatrix} 1 & \dots & 1 \\ \frac{-k+1}{2}\Delta t & \dots & \frac{k-1}{2}\Delta t \end{bmatrix} \begin{bmatrix} y_1 \\ \vdots \\ y_k \end{bmatrix}$$

$$\text{slope} = \frac{k}{k\Delta t^2 \frac{k^3-k}{12}} \begin{bmatrix} \frac{-k+1}{2}\Delta t & \dots & \frac{k-1}{2}\Delta t \end{bmatrix} \begin{bmatrix} y_1 \\ \vdots \\ y_k \end{bmatrix}$$

$$\text{slope} = \frac{1}{\Delta t \frac{k^3-k}{12}} \begin{bmatrix} \frac{-k+1}{2} & \dots & \frac{k-1}{2} \end{bmatrix} \begin{bmatrix} y_1 \\ \vdots \\ y_k \end{bmatrix}$$

Since the slope estimate is a linear combination of observed size values $Y = [y_1 \; y_2 \; \dots \; y_k]^T$, errors also propagate linearly. If all the size measurements have independent and identically distributed errors with mean zero and root-mean-square-error (RMSE) σ_ϵ, then the slope RMSE is σ_ϵ times the magnitude of the coefficient vector, $\frac{1}{\Delta t \frac{k^3-k}{12}} \begin{bmatrix} \frac{-k+1}{2} & \dots & \frac{k-1}{2} \end{bmatrix}$. The magnitude of $\begin{bmatrix} \frac{-k+1}{2} & \dots & \frac{k-1}{2} \end{bmatrix}$ is $\sqrt{\frac{k^3-k}{12}}$, therefore

$$\sigma_{\text{slope}} = \frac{\sigma_\epsilon \sqrt{12}}{\Delta t \sqrt{k^3-k}} \approx \frac{\sigma_\epsilon \sqrt{12}}{\Delta t k^{1.5}} \quad (2)$$

It is worth note that we could parameterize this instead in terms of total time transiting the array, $T = k\Delta t$, with k measurements occurring at evenly-spaced increments throughout this interval.

$$\sigma_{\text{slope}} \approx \frac{\sigma_\epsilon \sqrt{12}}{T \sqrt{k}}$$

In this form, it is clearly seen that the standard error scales inversely proportional to the total measurement duration, with a $\sqrt{k}$ dependence on the number of measurements made during that interval (in direct analogy to the central limit theorem).

We can use equation (2) generally to estimate the resolution of any sytem measuring rates of mass or volume increase, but specifically in the case of a serial SMR array, it also provides a convenient way to express the effect of the flow rate, which controls the trade-off between mass accumulation rate resolution and throughput. As we increase the flow rate, we decrease Δt proportionally, which decreases the mass accumulation rate resolution. Simultaneously, the throughput goes up directly proportionally to flow rate. An added effect is that faster flow rates yield larger *mass* error, σ_ϵ, as the cell spends a smaller amount of time in the cantilever and therefore cannot filter out as much frequency noise. For white-noise-dominated resonant frequency measurements (here corresponding to flow rates faster than what we've utilized in this paper for large-channel devices, e.g. $\Delta t < 2$ minutes), we expect that σ_ϵ will scale roughly inversely proportional to the square root of Δt:

$$\sigma_\epsilon = \frac{\alpha}{\sqrt{\Delta t}} \tag{3}$$

Plugging this into (2) suggests that as we increase the flow rate, the mass accumulation rate error is expected to scale with throughput $(1/\Delta t)$ to the three-halves.

$$\sigma_{\text{slope}} = \frac{\alpha\sqrt{12}}{\Delta t^{1.5}\sqrt{k^3 - k}} \tag{4}$$

We have illustrated this resolution-noise trade-off in Supplementary Figure 14. For slower flow, σ_ϵ may not be dominated by white frequency noise but instead by flicker (pink) or brown noise, and therefore (3) will sizably underestimate the actual mass noise magnitude.

Note 2: Mass sensitivity scales with frequency$^{3/2}$ for varied cantilever lengths

The cantilever resonant frequency f is given by $f = \frac{1}{2\pi}\sqrt{\frac{k}{m_{\text{eff}}}}$, where k is the spring constant and m_{eff} is the effective mass of the cantilever. m_{eff} is proportional to the cantilever length l [6], and k is proportional to $1/l^3$ [7], therefore $f \propto \frac{1}{l^2}$.

We can similarly determine how the cantilever mass sensitivity [8], s depends on length: $s \propto \frac{f}{m} \propto \frac{1}{l^3}$. Combining these two facts, we find s will be proportional to $f^{3/2}$, when all dimensional parameters other than the length of the cantilever are kept constant.

Note 3: Explanation of peak matching algorithm

We attempt to identify all the peaks (up to twelve, one in each cantilever) that we believe originate from the same cell. To do this, we use a heuristic approach in which we build "cells", collections of peaks that we believe belong to the same cell. At each cantilever in turn, starting at the second cantilever, we try to match the observed peaks at that cantilever with the previously observed cells. To match peaks to their corresponding cells, we define a cost function, detailed below, representing our assumptions about how cells both grow and flow through the device. We then try to find a way of pairing the already-observed cells (from the first n cantilevers) with the peaks observed at cantilever $n+1$ that minimally violates our expectations. Additionally, we also include the possibility that a cell is not observed at a particular cantilever, possibly due to simultaneously entering the cantilever at the same time as another cell, or adhering to the device walls. We include this possibility by adding fictitious cells ("gaps") such that a previously-observed cell can be assigned to a gap if there are no peaks at sensor n that are likely to originate from that cell. Similarly, a peak in cantilever $n+1$ can be assigned to a gap if it doesnt appear to clearly appear to correspond to an existing cell.

Pseudo-code for our matching approach is given below (variables are denoted in blue):

```
Initialize each peak in sensor 1 as its own cell, put them all in cellList

For each sensor n in 1:(numberOfSensors-1)
   peaksToBeAssigned = all peaks in sensor n+1

   costs = matrix( number of rows = length(cellList),
                   number of columns = length(peaksToBeAssigned) )
   Pad costs with extra rows and columns for 'unassigned' cells
   Set entries of costs for assigning a cell to 'unassigned' to gapCost
   Set entries of costs for assigning 'unassigned' to 'unassigned' to 0

   For each r in 1:length(cellList)
      For each c in 1:length(peaksToBeAssigned)
         costs[r,c] = -log( P(peaksToBeAssigned[c] | cellList[r]) )

   Find optimal assignment for costs via Hungarian algorithm

   Any peaks in peaksToBeAssigned that were assigned to existing cells in the cellList
   should be concatenated onto the end of their corresponding cell.

   Any entries in peaksToBeAssigned NOT assigned to existing cells are added to the
   cellList as cells containing only one peak.
```

The heart of this approach is how we define a cost function representing our prior assumptions about device behavior (e.g. cells take approximately two minutes to transit from one cantilever to the next, and can't possibly show up at cantilever 2 before appearing at cantilever 1) and cell behavior (over such a short time period, cell mass usually changes roughly linearly, and the rate of change is unlikely to be extremely large). To represent these assumptions, we use a probabilistic model of seeing a peak of a particular mass and time at sensor $n+1$, given the previous n peaks we've already decided are part of the cell's trajectory. Using the negative log of the probability gives us a cost function for which minimizing the cost corresponds to maximizing the likelihood of the data.

We model the probability of observing a peak of mass m_{n+1} and at time t_{n+1}, conditioned on the peak occurring at sensor $n+1$ and having observed previous peaks of masses $m_{1:n}$ at times $t_{1:n}$, as follows:

$$P(m_{n+1}, t_{n+1}|m_{1:n}, t_{1:n}) = P(m_{n+1}|t_{n+1}, m_{1:n}, t_{1:n})P(t_{n+1}|m_{1:n}, t_{1:n})$$

We then assume t_{n+1} depends only on t_n, and is normally distributed with mean $t_n + \mu_{\Delta t}$ and variance $\sigma^2_{\Delta t}$, where $\mu_{\Delta t}$ and $\sigma^2_{\Delta t}$ are specified by the user *a priori*. We further posit that m_{n+1} should be related to t_{n+1} and the previous data via the following relation

$$m_{n+1} = \beta_1 t_{n+1} + \beta_0 + \epsilon$$

where β_1 is a random variable corresponding to the slope implied by the previous datapoints, β_0 is the y-intercept, and ϵ is random instrument noise. If we mean-center the time values ($\sum_{i \in 1:n} t_i = 0$), then β_0 and β_1 become uncorrelated, and we can thus express the mean and variance of m_{n+1} as

$$\mu_{m_{n+1}} = t_{n+1}\mu_{\beta_1} + \mu_{\beta_0}$$
$$\sigma^2_{m_{n+1}} = t^2_{n+1}\sigma^2_{\beta_1} + \sigma^2_{\beta_0} + \sigma^2_{\epsilon}$$

Furthermore, if β_1, β_0 and ϵ are assumed normal, then m_{n+1} is normally distributed with the above parameters.

While it is straightforward to obtain frequentist estimates of β_1 and $\sigma^2_{\beta_1}$ when we have already seen many datapoints, we cannot estimate these quantities easily with only one or two datapoints. To mitigate this we use Bayesian estimators, which are shaped by a prior distribution when only one or a few datapoints are available, and shaped more by the data when more data becomes available. The conjugate prior for β_1 is normal (assuming the mass sensor error parameter σ_ϵ is already known) and is specified by hyper-parameters $\overline{\mu}_{\beta_1}$ and $\overline{\sigma}^2_{\beta_1}$. The posterior distributions for β_1 is also normal, with variance and mean as follows:

$$\sigma^2_{\beta_1} = \frac{1}{\frac{1}{\overline{\sigma}^2_{\beta_1}} + \frac{t_{1:n} \cdot t_{1:n}}{\sigma^2_\epsilon}}$$

$$\mu_{\beta_1} = \sigma^2_{\beta_1}\left(\frac{\overline{\mu}_{\beta_1}}{\overline{\sigma}^2_{\beta_1}} + \frac{t_{1:n} \cdot m_{1:n}}{\sigma^2_\epsilon}\right)$$

We also assume that since σ_ϵ is known, μ_{β_0} is just the mean mass from the n previous observations, and $\sigma^2_{\beta_0} = \sigma^2_\epsilon/n$. Using these parameters, we can then write the cost function as:

$$\text{Cost}(m_{n+1}, t_{n+1}|m_{1:n}, t_{1:n}) = -\log\left[N(m_{n+1}|\mu_{m_{n+1}}, \sigma^2_{m_{n+1}})\right] - \log\left[N(t_{n+1}|t_n + \mu_{\Delta t}, \sigma^2_{\Delta t})\right] \quad (5)$$

where $N(x|\mu,\sigma^2)$ is the normal density function evaluated at x with mean μ and variance σ^2. Examples of this cost function for simulated cells are shown in Supplementary Figure 4, demonstrating how this cost function narrows as more and more data is observed.

In sum, the cost depends on the new data (m_{n+1}, t_{n+1}), the previously observed data ($m_{1:n}$, $t_{1:n}$), and five user-defined parameters:

parameter	description
σ	sensor RMS error
$\overline{\mu}_{\beta_1}$	prior expectation for mean mass accumulation rate
$\overline{\sigma}^2_{\beta_1}$	prior expectation for mass accumulation rate variance
$\mu_{\Delta t}$	expected average time between sensors
$\sigma^2_{\Delta t}$	expected variance in time between sensors

Additionally, there is one more parameter for the cost of a gap, yielding six parameters in total controlling the matching process.

It is worth note that by simply choosing the best matching between the previously-observed cells and the newly-observed peaks at every step, we do not properly take into account uncertainty in the matching process. While we have not undertaken this task here, future work to do so may utilize Murty's algorithm [9] to obtain not only the optimal assignment (as provided by the Hungarian algorithm), but a ranked set of the best assignments (e.g. the top 50 assignments). This would allow one to check which assignments are tenuous and which are very certain.

Note 4: Comparison of measurement precision between SMRs and quantitative phase microscopy (QPM)

Comparisons of SMR and QPM mass measurements cannot be made directly because the two methods exploit different physical principles. QPM requires computing an unwrapped phase shift function from image data to yield optical thickness. Optical thickness is integrated over the area of a cell, and the result is multiplied by a constant to convert it into dry mass units. The constant is based on an average refractive increment of mostly globular proteins [10]. On the other hand, SMR measurements are based on the change in resonant frequency of an oscillating cantilever caused by a cell passing through an embedded microfluidic channel. The frequency shift is divided by a sensitivity constant (Hz/pg) to obtain buoyant mass. The sensitivity constant is a device parameter and independent of the properties of the analytes. It is obtained by direct calibration with particles of known buoyant mass.

Supplementary Figures 13A and 13C show mass measurements of *E.coli* cells with similar interdivision times made by QPM (left panel) and SMR (right panel). The left panel shows dry mass versus time for three *E. coli* cells measured by Mir et al. using QPM [3]. Buoyant mass versus time for 11 *E. coli* cells measured by SMR is shown on the right. Buoyant mass error for these cells is 0.22 fg, based on repeat measurements of a single inert polystyrene particle similar in size and density to these cells (1.36 μm diameter, 1.05 g/mL). One way to compare the precision of the two methods is to convert the SMR buoyant mass to dry mass. This is possible using a method we validated in a previous study [11]. Briefly, we measured the buoyant mass of *E. coli* cells in two fluids with different densities. The first fluid was a standard phosphate-buffered saline solution. The second fluid was identical to the first, except the water in the formula was replaced by heavy water (D_2O). Using the method of Archimedes, we found the density of *E. coli* biomass (*E. coli*'s dry density) to be 1.45 g/mL. This constant can be used to convert buoyant mass to dry mass, as shown on the right axis in Supplementary Figure 13C. The conversion produces good agreement between the *E. coli* dry mass obtained by the two methods. Converting buoyant mass error to dry mass error yields an error of 0.63 fg, approximately 30 times smaller than values produced by QPM.

Another way to assess the precision of the two methods is to compare the relative uncertainties of both techniques. Because they are unitless, relative uncertainties can be compared directly. In Mir et al. [3], measurements of a ~1.5 pg cell dry mass have a standard deviation of ~0.0196 pg, yielding a relative uncertainty of 1.3%. SMR measurements of similarly-sized cells with an average buoyant mass around 0.3 pg have a standard deviation of 0.20 fg, or 0.06% relative uncertainty, about 20 times better precision than QPM. Both the dry mass conversion and relative uncertainty approaches give similar values.

We also find that serial and single SMR measurements of mass accumulation rates exhibit less variation than those measured by QPM. Supplementary Figures 13B and 13D compare mass accumulation rate measurements obtained by QPM and SMR. The left panel (Supplementary Figure 13B) shows dry mass accumulation rate (referred to as growth rate) vs. dry mass of 20 cells measured in reference [3]. Supplementary Figure 13D shows two analogous datasets produced by the SMR method - one taken with a single SMR device at low throughput and another taken on a serial SMR array with a higher flow rate.

How does the noise of the single SMR compare to the serial SMR array results shown in Figure 6 and Supplementary Figure 13? The uncertainty in SMR buoyant mass measurements depends on the flow rate of cells through the device. By varying the flow rate, the system can be optimized for throughput or measurement precision. The noise level in the serial SMR array measurements (Figure 6) is about 3 times higher than the single SMR in Supplementary Figure 13C because of the faster flow rate. This could be reduced at the expense of lower throughput.

References

[1] S. Olcum, N. Cermak, S. C. Wasserman, and S. R. Manalis, "High-speed multiple-mode mass-sensing resolves dynamic nanoscale mass distributions," *Nat Commun*, vol. 6, May 2015.

[2] E. Gavartin, P. Verlot, and T. J. Kippenberg, "Stabilization of a linear nanomechanical oscillator to its thermodynamic limit," *Nat Commun*, vol. 4, Dec. 2013.

[3] M. Mir, Z. Wang, Z. Shen, M. Bednarz, R. Bashir, I. Golding, S. G. Prasanth, and G. Popescu, "Optical measurement of cycle-dependent cell growth," *Proc Natl Acad Sci USA*, vol. 108, pp. 13124–13129, Aug. 2011.

[4] M. Godin, F. F. Delgado, S. Son, W. H. Grover, A. K. Bryan, A. Tzur, P. Jorgensen, K. Payer, A. D. Grossman, M. W. Kirschner, and S. R. Manalis, "Using buoyant mass to measure the growth of single cells," *Nat Meth*, vol. 7, pp. 387–390, Apr. 2010.

[5] D. Wackerly, W. Mendenhall, and R. L. Scheaffer, *Mathematical Statistics with Applications*. Belmont, CA: Thomson Brooks/Cole, 7 ed., 2008.

[6] A. Cleland, *Foundations of Nanomechanics: From Solid-State Theory to Device Applications*. Advanced Texts in Physics, Springer Berlin Heidelberg, 2002.

[7] S. P. Timoshenko and J. M. Gere, *Mechanics of Materials*. New York: Van Nostrand Reinhold Co., 1 ed., 1972.

[8] K. L. Ekinci, Y. T. Yang, and M. L. Roukes, "Ultimate limits to inertial mass sensing based upon nanoelectromechanical systems," vol. 95, no. 5, pp. 2682–2689.

[9] K. G. Murty, "Letter to the Editor - An Algorithm for Ranking all the Assignments in Order of Increasing Cost," *Operations Research*, vol. 16, pp. 682–687, June 1968.

[10] R. Barer, "Refractometry and Interferometry of Living Cells," *J. Opt. Soc. Am.*, vol. 47, pp. 545–556, June 1957.

[11] F. Feijó Delgado, N. Cermak, V. C. Hecht, S. Son, Y. Li, S. M. Knudsen, S. Olcum, J. M. Higgins, J. Chen, W. H. Grover, and S. R. Manalis, "Intracellular water exchange for measuring the dry mass, water mass and changes in chemical composition of living cells," *PLoS ONE*, vol. 8, no. 7, p. e67590, 2013.